Chapter 4

Numerical Modeling of Smart Foam

4.1 Introduction

Porous bodies are aggregates of solid elements between which voids form the pore space itself. These voids within the porous body give rise to the wide differences in physical behavior between dense solids and porous substances, which are assemblages in which the presence of the fluid adds to the overall complexity of the material [41]. In a broad classification, porous materials can be described as either rigid framed or elastic framed materials. Examples of rigid framed porous media are honeycomb core which consists of narrow cavities that act as resonators and porous rock. Fiberglass and acoustical foams are considered elastic framed porous materials. All of these materials are heterogeneous in that they are comprised of a solid phase (often referred to as the frame) and a fluid phase (see Figure 4.1). In dealing with the problem of acoustic wave propagation in saturated, porous media for dynamic analysis of the subsurface, two approaches are possible. The first approach is based on the homogenization principle [42] which links the microscopic and macroscopic laws of sound propagation. The term microscopic applies to laws governing mechanisms at the scale of heterogeneity. Macroscopic laws refer to a scale related to the heterogeneous medium concerned. The second approach consists of deliberately ignoring the microscopic level and assuming that

the concepts and principles of continuum mechanics can be applied to obtain measurable macroscopic values. For this work, the author has decided to present an analysis of porous media using a macroscopic approach since it has more physically realizable assumptions. As illustrated in Figure 4.1, the basic premise of the theory requires that there exists a macroscopic elementary volume or subdomain that is representative of the porous media considered. The basic premise is that the pore size (d) is much smaller than the macroscopic elementary volume of porous material (D_1). It is also assumed that the wavelength (D_2) of sound propagating within the porous layer is much larger than the pore space and the macroscopic elementary volume. Accordingly, it is possible to establish average volume displacements per unit cross sectional area for the solid phase $\{u_x\ u_y\ u_z\}$ and the fluid phase $\{U_x\ U_y\ U_z\}$ of the porous layer which are common, easily-handled physical properties.

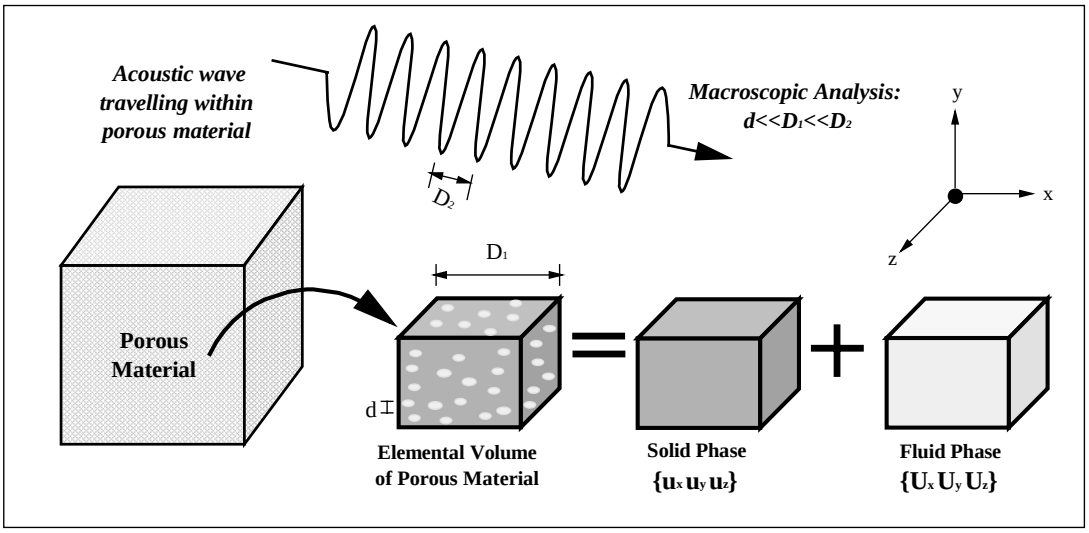

Figure 4.1 Illustration of a generic porous material and the macroscopic modeling approach.

Porous acoustical materials are unique in that air represents the fluid phase of the material. Acoustical foam, which is an essential component in this study can be described by several macroscopic parameters. These parameters are the porosity, flow resistance, the tortuosity, bulk density, Young's modulus with associated loss factor and Poisson's

ratio. A description of some of these parameters and suggested measurement techniques [43,44,45,46] are given in Table 4.1.

Table 4.1 Important foam parameters and measurement techniques.

Foam Property & Definition	Measurement Technique
Porosity: ratio of air volume/total volume of porous material	pore volume measured directly by the difference in dry and saturated weight in a vacuum
Flow resistivity: resistance to air flow per unit thickness	foam sample placed in a pipe; differential pressure induced by a steady flow of air
Tortuosity: describes pores deviation from straight cylindrical passages	compare electrical conductivity of a conductive fluid with that of the foam sample saturated by the same fluid
Young's modulus & associated loss factor: stiffness of foam	compute the flexural response of a beam with and without the foam attached

There are three categories of porous acoustical foams. The categories are open cell, partially-reticulated and closed cell foams. These three types are distinguished from each other by the degree to which the cell membranes are removed during the manufacturing process. The cell membranes are completely extracted in open cell foams. Open cell foams tend to be quite limp and little coupling exists between the motion of the solid and fluid phases. An example of an open cell foam is fiberglass which is commonly used for building insulation. In partially-reticulated foams, only a portion of the cell membranes are removed, the fluid propagation path tends to follow tortuous passages. Partial foam reticulation results in an elevated frame stiffness and Poisson's ratio in comparison to open cell foams. A large tortuosity reduces the phase speed of the airborne waves, but also increases the viscous and inertial effects that are present due to the strong coupling between the motion of the solid phase and the interstitial fluid. Polyurethane acoustical foam is an example of partially-reticulated porous material. Closed cell foams are airtight and all the fluid is trapped within closed cells. They resemble homogeneous elastic medium. Generally, poor acoustical properties are offered by closed cell foams. Owing to these facts, noise control applications employ partially-reticulated acoustic foams as passive sound absorbers in the high frequency range where the dissipative mechanisms within the foam are significant [47, 48].

4.2 Overview of Poroelastic Material Theory Development

The following discussion summarizes the work of key contributors in the evolvement of theories related to wave propagation in poroelastic media. A complete listing is beyond the scope of this thesis, however, a general historical description of previous work is necessary in the interest of completeness.

In 1896, Rayleigh [49] presented the first published material on sound propagation in air-saturated, porous media. He investigated the performance of an idealized absorber of sound, consisting of a bundle of small tubes aligned in the direction of wave propagation. He extended the theories of Helmholtz and Kirchoff that relate to the transmission of sound along tubes and was able to deduce a value for the absorption coefficient at the surface of the absorber in terms of the proportion of the surface area occupied by open pores, the radius of the tubes and the physical constants of the air. Although the solid component of the material was assumed to be rigid, this simple model accounted for viscous and thermal losses in the pores which is a key feature in modern models.

Zwikker & Kosten [50] were perhaps the earliest scientists to study sound absorbing elastic materials. Unlike Rayleigh, they accounted for the possibility of vibration of the solid material and addressed the mathematical problem of the coupled vibrations of the solid and fluid phases. The phase coupling is attributed to fluid viscosity and inertial effects created by a pore structure that deviated from straight cylindrical passages. The Zwikker and Kosten approach predicts the presence of two longitudinal wave types that are common to each phase of the porous material.

In 1956, Biot [51, 52, 53] advanced the theory of Zwikker and Kosten to describe wave propagation in media related to geophysics. The model included shear stiffness of the solid phase of an elastic porous material. Accordingly, the Biot theory predicted the presence of two longitudinal wave types and one shear wave type in porous, elastic media. It is the most general, elastic porous material theory available. Seven constitutive equations are derived that relate stress and pressure in the frame and the fluid to the coupled deformations of both phases. The constitutive equations are expressed in terms of two Lame' coefficients and two coupling coefficients. The viscous and inertial

coupling effects are included in three effective densities. Six equations govern the motion of the frame and fluid in three orthogonal directions.

Delaney & Bazely [54] presented empirical methods that have been widely used for predicting sound propagation in various grades of fibrous materials. These laws have been used in various applications such as sound attenuation in ducts, room acoustics, the calculation of transmission loss through walls, and primarily models describing sound propagation above various types of ground. The geometry of fibrous materials was not taken into account.

The subject of shape factors as applied to the pore geometry of rigid porous materials is addressed by Champoux and Stinson [55]. They accurately predicted the complex density and propagation constant in rigid-framed porous materials having large variations in pore cross-sectional area. They introduced the use of shape factors to treat the effect of pore shape on the thermal and viscous functions. It is demonstrated that the dynamic density function (that describes the viscous effects) is associated more with the narrow sections of the pores and the dynamic bulk modulus (describing the thermal effects) is associated more with the wider sections of the pores. Two different shape factors are required, in general, to describe both the viscous and thermal effects. Very good agreement between the experimental results and the theoretical predictions is found.

Attenborough [56] and Johnson et al. [57] have also contributed significantly to the study of rigid porous materials with attention given to pore geometry.

Works by Allard [58, 59] were developed to adapt specifically the Biot theory to acoustics problems involving mutilayered poroelastic media. His model includes two characteristic dimensions for viscosity and the bulk modulus of air within the pores, respectively. These parameters are dependent on the foam material properties and pore shape factors.

Bolton et al. [60,61,62] published analytical studies based on the Biot theory which deal with normal and oblique wave propagation in elastic porous materials with it’s application to the prediction of the transmission loss of foam lined noise control treatments.

Early work related to absorptive finite elements was performed by Craggs [63, 64] and related to lined rectangular rooms. The theory was derived from a generalized Rayleigh model, but allowed for a frequency dependent flow resistivity and density. It also considered the effects of porosity. The application of the theory shows good agreement with experimental data taken for foam material and with the empirical formula developed by Delaney and Bazely for effectively rigid materials. These comparisons were carried out for normal incidence only and accounted for only one wavetype. It is now known that three distinct wavetypes (i.e. two longitudinal and one shear wave) contribute significantly to the acoustical behavior of poroelastic materials such as foams. Therefore, Cragg's approach is not appropriate for noise control foams.

Recently, Kang [65, 66] presented an elastic-absorption finite element model of isotropic elastic porous noise control materials implementing a finite element approach. The two-dimensional displacement based approach is founded on the Biot theory and allows for the propagation of the three types of waves known to propagate in a poroelastic material. The starting point of this formulation was the differential equations of dynamic equilibrium. Next, the discretized poroelastic equations were derived using Galerkin's method. A method of coupling foam and acoustic finite elements is presented. The effects of finite dimension and edge constraints on sound absorption and transmission through layers of acoustical foam is studied. Good agreement is achieved when finite element predictions are compared with established analytical plane wave absorption and transmission loss.

Panneton [67, 68, 69] employed the finite element method to solve the three dimensional poroelasticity problem related to sound absorption and transmission loss based on the Biot theory. His work differs from Kang's in that it is derived using a Lagrangian approach. Furthermore, he gives attention to the efficiency (i.e. solution time and memory requirements) of the numerical implementation by introducing realistic approximations to remove the complex nature and frequency dependence of the poroelastic material properties.

4.3 Biot Theory of Sound Propagation in Isotropic, Elastic Porous Materials

The purpose of the present discussion concerning the analytical modeling of sound wave propagation in porous materials undergoing an acoustic excitation is twofold. Firstly, the model serves to identify the unique characteristics of porous materials. It is shown that the presence of the fluid phase significantly effects the behavior of the material when compared to a similar elastic, homogeneous medium. Two compressional waves and one shear wave can travel within the foam. Derivation of the complex wavenumbers, allows the phase speed and attenuation coefficient of each wavetype to be studied as a function of frequency. The second function of the analytical formulation of porous materials is to validate the finite element model. This will be accomplished by comparing the acoustic impedance of partially-reticulated acoustic foam predicted by each approach.

The theory describing acoustic wave propagation in an elastic porous material filled with compressible viscous fluid is considered in the context of Biot theory as presented by Allard [59]. As stated previously, this macroscopic approach utilizes the concepts and principles of continuum mechanics [70] to obtain measurable macroscopic values describing the dynamic behavior of the material. The major hypotheses of the Biot theory are:

- *the poroelastic subdomains are homogeneous and isotropic.*
- *the wavelength is large in comparison with the dimensions of the macroscopic elementary volume.*
- *the pore space is small relative to the macroscopic elementary volume.*
- *deformations are small which guarantee linearity of the mechanical processes.*
- *viscous damping and heat transfer at the pore walls is considered.*
- *the fluid within the pores is initially at rest and the flow of fluid relative to the solid is of Poiseuille type (i.e. the instantaneous velocity profile is parabolic).*

After defining the stress-strain relations for both the solid phase and fluid phase and the potential and kinetic energy expressions, the three dimensional dynamic equations of motion are derived using Lagrange's equations [71]. These equations contain three effective mass coefficients reflecting the inertial coupling between the solid and fluid

phase and the viscous dissipation present in the porous material. Biot theory identifies the existence of two compressional waves and one shear wave.

4.3.1 Stress-Strain Relations

In an elastic solid or in a fluid, stresses are defined as being tangential or normal forces per unit area of material. The same definition will be used for porous materials, and stresses are defined as being forces acting on the frame or the air per unit area of porous material as illustrated in Figure 4.2.

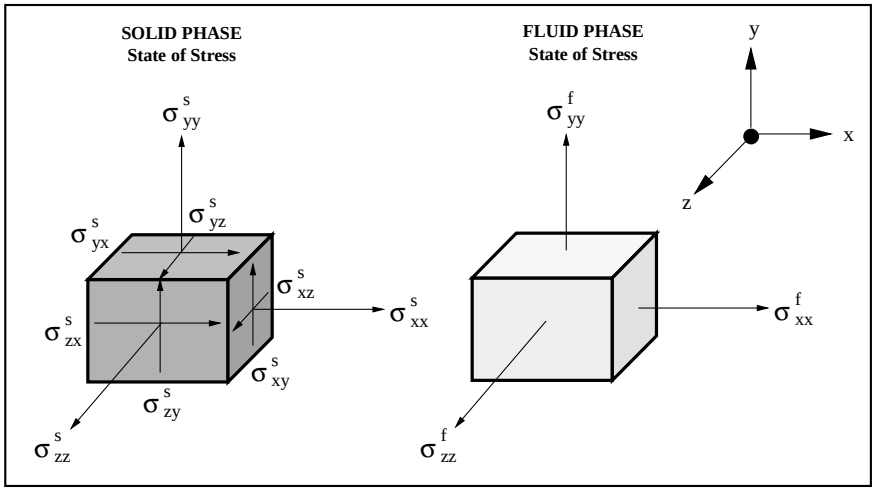

Figure 4.2 State of stress in the solid and fluid phases of an elementary macroscopic volume of porous material.

As a consequence, the stress tensor components for the solid are

$$\sigma^s = \left\{\sigma^s_{xx}\ \sigma^s_{yy}\ \sigma^s_{zz}\ \sigma^s_{xy}\ \sigma^s_{yz}\ \sigma^s_{zx}\right\} \tag{1}$$

The forces acting on the fluid part of each face of the cube are represented by

$$\sigma^f = \left\{\sigma^f_{xx}\ \sigma^f_{yy}\ \sigma^f_{zz}\ \ 0\ 0\ 0\right\} \tag{2}$$

The fluid stress components can be succinctly described by

$$\sigma_{ij} = -\beta p \delta_{ij} \tag{3}$$

where p denotes the pressure and β denotes the fraction of fluid area per cross section, and δ_{ij} is the Kronecker symbol defined as

$$\delta_{ij} = \begin{cases} 0 & if\ i \neq j \\ 1 & if\ i = j \end{cases} \tag{4}$$

Note that σ^f is taken negative when the force acting on the fluid is a pressure, and σ^s is positive when the force in the solid is a tension. It is important to call attention to the significance of the factor β. In this analysis, it is assumed that we are dealing with a statistically isotropic porous material in such a way that for all cross sections, the same ratio of fluid area to solid area is observed. Hence the volume of fluid in a thin slab of thickness dx is always a fraction β of the total volume. This means that β is identical to the porosity, ϕ, or the ratio of fluid volume to total volume of the material. It is important to note that $\sigma^p = \sigma^s + \sigma^f$ or the total stress tensor of the poroelastic material is the sum of the tensor related to the solid and fluid phase, respectively.

The strain tensor in the solid is denoted by

$$\varepsilon^s = \left\{\varepsilon^s_{xx}\ \varepsilon^s_{yy}\ \varepsilon^s_{zz}\ 2\varepsilon^s_{xy}\ 2\varepsilon^s_{yz}\ 2\varepsilon^s_{zx}\right\} \tag{5}$$

where

$$\varepsilon^s_{ij} = \frac{1}{2}\left(u_{i,j} + u_{j,i}\right) \tag{6}$$

We may also define the dilatation of the solid phase as

$$\theta^s = u_{i,i} \tag{7}$$

where u={u_x u_y u_z} is the displacement vector of the solid. Keep in mind that the displacement vector is defined as the displacement of the material which is considered to be uniform and averaged over the element. Similarly, the average fluid displacement vector U={U_x U_y U_z} is defined so that the product of this displacement with the cross-sectional fluid area represents the volume flow. The strain in the fluid is defined as

$$\varepsilon^f = \left\{\varepsilon^f_{xx}\ \varepsilon^f_{yy}\ \varepsilon^f_{zz}\ 0\ 0\ 0\right\} \tag{8}$$

where

$$\varepsilon^f_{ij} = U_{k,l}\,\delta_{ik}\,\delta_{jk}\,\delta_{kl} \tag{9}$$

and the fluid dilatation is

$$\theta^f = U_{i,i} \tag{10}$$

It is important to note that $\varepsilon^p = \varepsilon^s + \varepsilon^f$ or the total strain of the poroelastic material is the sum of the tensor related to the solid and fluid phase, respectively, and has seven components.

It is now necessary to establish a relationship between the stress and strain components of the poroelastic material. Disregarding all dissipative forces and assuming that the material is a conservative physical system which is in equilibrium when at rest, any deformation is therefore a departure from the state of minimal potential energy. The potential energy can be expressed by a positive definite quadratic form where the stress components will then be linear functions of the six strain components. The potential energy W per unit of material is given by

$$W = \frac{1}{2}\left(\sigma_{ij}^s \varepsilon_{ij}^s + \sigma_{ij}^f \varepsilon_{ij}^f\right) \tag{11}$$

The stress-strain relations may be expressed as

$$\begin{aligned} \sigma_{ij}^s &= \frac{\partial W}{\partial \varepsilon_{ij}^s} \\ \sigma_{ij}^f &= \frac{\partial W}{\partial \varepsilon_{ij}^f} \end{aligned} \tag{12}$$

The seven by seven matrix of coefficients in the foregoing set of linear relations constitute a symmetric matrix with twenty eight distinct coefficients [53]. These relations are very much simplified if the assumption that the solid-fluid system is statistically isotropic. In this case, the principal stress and principal strain directions coincide and the stress-strain relations can be written for arbitrary directions as

$$\sigma_{ij}^s = \left(A\theta^s + Q\theta^f\right)\delta_{ij} + 2N\varepsilon_{ij}^s\delta_{ij} \tag{13a}$$

$$\sigma_{ij}^f = \left(Q\theta^s + R\theta^f\right)\delta_{ij} = -\phi p\delta_{ij} \tag{13b}$$

In examining the significance of the coefficients of equations (13a,b), the terms A and N correspond to the familiar Lame coefficients in the theory of elasticity and are of positive sign. The coefficent N denotes the shear modulus of the material. The quantity Q gives the contributions of the air dilatation to the stress in the frame, and of the frame dilatation to the pressure variation in the air in the porous material. The quantity Q is the potential coupling coefficient**.** The quantity R relates the fluid stress and strain. The

"gedanken experiments", performed by Biot et al. [72] provide an evaluation of the elasticity coefficients A, N, Q and R. In the experiments, the material is subjected to pure shear to establish the shear modulus of the solid phase. The other experiments determine the expressions of A, Q and R as a function of three significant physical properties of the material. These properties are the bulk modulus of the material *in vacuo* (K_b), the bulk modulus of the elastic solid from which the frame is made (K_s), and the bulk modulus of the air (K_f). For porous materials saturated by air, it is practical to assume that $K_b/K_s<<<1$ and $K_f/K_s<<<1$. Accordingly, using Allard's notation the elasticity coefficients can be described in terms of K_b and K_f such that

$$A = \frac{4}{3}N + K_b + \frac{(1-\phi)^2}{\phi}K_f \tag{14}$$

$$Q = K_f(1-\phi) \tag{15}$$

and

$$R = \phi K_f \tag{16}$$

The rigidity of an elastic solid is commonly characterized by a shear modulus and the Poisson's ratio of the material. With regard to this, the bulk modulus K_b in equation (14) can be evaluated by the following expression

$$K_b = \frac{2N(\nu+1)}{3(1-2\nu)} \tag{17}$$

The terms N and ν represent the shear modulus and the Poisson coefficient, respectively. The bulk modulus of the fluid phase is defined by

$$K_f = \frac{\gamma P_o}{\gamma - (\gamma-1)\left[1 + \frac{8\eta}{j\Lambda'^2 B^2 \omega \rho_o}\sqrt{1 + j\frac{\Lambda'^2 B^2 \rho_o \omega}{16\eta}}\right]^{-1}} \tag{18}$$

where P_o is the atmospheric pressure, γ denotes the specific heat ratio, η is the viscosity of the air, ρ_o is the density of the air, σ is the mean flow resistance, B^2 is the Prandtl number and ω is the circular frequency. The value Λ' denotes the characteristic dimension for thermal effects and accounts for pore geometry.

4.3.2 Kinetic Energy Density

The kinetic energy of the system per unit volume, using the average velocity components as generalized coordinates, is expressed as

$$T = \frac{1}{2}\left\{\rho_{11}\left[\left(\dot{u}_x\right)^2 + \left(\dot{u}_y\right)^2\right] + 2\rho_{12}\left[\dot{u}_x\dot{U}_x + \dot{u}_y\dot{U}_y\right] + \rho_{22}\left[\left(\dot{U}_x\right)^2 + \left(\dot{U}_y\right)^2\right]\right\} \quad (19)$$

Note that the dot over u and U signify the first time derivative of the variable. The kinetic energy expression is based on the fact that the material is statistically isotropic, therefore, the orthogonal directions are equivalent and uncoupled dynamically. In equation (19), the mass coefficients ρ_{11} and ρ_{22} are related to the mass density of the solid and the fluid phases, respectively. The coefficient ρ_{12} considers the inertial interaction between both phases. These coefficients are defined as

$$\begin{aligned} \rho_{11} &= \rho_1 - \rho_{12} \\ \rho_{22} &= \phi\rho_o - \rho_{12} \\ \rho_{12} &= -\phi\rho_o\left(\alpha_o - 1\right) \end{aligned} \quad (20)$$

where α_o denotes the tortuosity of the material and ρ_1 .represents the density of the homogeneous solid phase of the foam.

4.3.3 Dissipation Function

As stated earlier, it will be assumed that the flow of fluid relative to the solid through the pores is of the Poiseulle type. The dissipation function may be written in a homogenous quadratic form. Because of the assumed statistical isotropy, orthogonal directions are uncoupled. The dissipation also vanishes when there is no relative motion between the fluid and solid. The dissipation function is defined as

$$D = \frac{1}{2}b\left\{\left(\dot{u}_x - \dot{U}_x\right)^2 + \left(\dot{u}_y - \dot{U}_y\right)^2\right\} \quad (21)$$

where the damping constant is given as

$$b = \phi^2\sigma\sqrt{1 + j\frac{4\alpha_\infty^2\eta\rho_o\omega}{\sigma^2\Lambda^2\phi^2}} \quad (22)$$

and Λ is the characteristic dimension for viscous forces taking into account pore geometry. Also, the term α_∞ denotes the limit of the tortuosity as ω tends to infinity.

4.3.4 Equations of Motion for an Isotropic, Elastic Porous Material

Lagrange's equations with viscous dissipation are denoted by

$$\frac{\partial}{\partial t}\left(\frac{\partial T}{\partial \dot{u}_i}\right)+\left(\frac{\partial D}{\partial \dot{u}_i}\right)=q_i \tag{23a}$$

$$\frac{\partial}{\partial t}\left(\frac{\partial T}{\partial \dot{U}_i}\right)+\left(\frac{\partial D}{\partial \dot{U}_i}\right)=Q_i \tag{23b}$$

The terms q_i and Q_i represent the elastic forces for the solid and fluid phase, respectively, such that

$$q_i=\frac{d}{dx_j}\frac{\partial \bar{W}}{\partial \varepsilon_{ij}^s}=\sigma_{ij,j,i}^s \tag{24a}$$

$$Q_i=\frac{d}{dx_j}\frac{\partial \bar{W}}{\partial \varepsilon_{ij}^f}=\sigma_{ij,j}^f=-\phi p_{,i} \tag{24b}$$

Substituting equations (19),(21) ,(24) into equations (23) yields

$$\sigma_{ij,j}^s=\left(\rho_{ii}\ddot{u}_i+\rho_{i2}\ddot{U}_i\right)+b\left(\dot{u}_i+\dot{U}_i\right) \tag{25a}$$

$$-\phi p_{,j}=\left(\rho_{12}\ddot{u}_i+\rho_{22}\ddot{U}_i\right)-b\left(\dot{u}_i+\dot{U}_i\right) \tag{25b}$$

Employing equations (6), (7), (9) and (10) and equation (13) in equation (25), we derive the equations of dynamic equilibrium in terms of the solid and fluid phase displacement such that

$$Nu_{i,jj}+(A+N)u_{j,ii}+QU_{j,ii}=-\omega^2\left(\tilde{\rho}_{11}u_i+\tilde{\rho}_{12}U_i\right) \tag{26a}$$

$$Qu_{i,jj}+Ru_{j,ii}+QU_{j,ii}=-\omega^2\left(\tilde{\rho}_{12}u_i+\tilde{\rho}_{22}U_i\right) \tag{26b}$$

where harmonic motion having an $e^{j\omega t}$ time dependence is assumed. In the above equations,

$$\tilde{\rho}_{11} = \rho_{11} - j\frac{b}{\omega}$$
$$\tilde{\rho}_{22} = \rho_{22} - j\frac{b}{\omega} \tag{28}$$
$$\tilde{\rho}_{12} = \rho_{12} + j\frac{b}{\omega}$$

These parameters take into account the inertial effects and viscous dissipation of the porous material.

4.4 The Compressional Waves

As in the case of an elastic solid, the wave equations of the compressional and rotational waves can be obtained by using scalar and vector displacement potentials, respectively. Two scalar potentials for the frame and the air, Φ^s and Φ^f, are defined for the compressional waves, giving

$$u = \nabla\Phi^s \tag{28a}$$

$$U = \nabla\Phi^f \tag{28b}$$

By employing the relation $\nabla\nabla^2\Phi = \nabla^2\nabla\Phi$ in equations (26a) and (26b), it can be shown that Φ^s and Φ^f are related as follows:

$$\begin{aligned} -\omega^2\left(\tilde{\rho}_{11}\Phi^s + \tilde{\rho}_{12}\Phi^f\right) &= P\nabla^2\Phi^s + Q\nabla^2\Phi^f \\ -\omega^2\left(\tilde{\rho}_{22}\Phi^f + \tilde{\rho}_{12}\Phi^s\right) &= R\nabla^2\Phi^f + Q\nabla^2\Phi^s \end{aligned} \tag{29}$$

where

$$P = A + 2N \tag{30}$$

The two scalar potentials may be used to define the following vector

$$[\Phi] = \left[\Phi^s \;\; \Phi^f\right]^T \tag{31}$$

Equations (29) can then be reformulated as

$$-\omega^2[M]^{-1}[\rho][\Phi] = \nabla^2[\Phi] \tag{32}$$

where

$$[\rho] = \begin{bmatrix} \tilde{\rho}_{11} & \tilde{\rho}_{12} \\ \tilde{\rho}_{12} & \tilde{\rho}_{22} \end{bmatrix}, \qquad [M] = \begin{bmatrix} P & Q \\ Q & R \end{bmatrix} \tag{33}$$

Allow δ_1^2 and δ_2^2 to define the eigenvalues, and $[\Phi_1]$ and $[\Phi_2]$ the eigenvectors, of the left-hand side of equation (32). These quantities are related by

$$\begin{aligned} -\delta_1^2[\Phi_1] &= \nabla^2[\Phi_1] \\ -\delta_2^2[\Phi_2] &= \nabla^2[\Phi_2] \end{aligned} \tag{34}$$

The eigenvalues δ_1^2 and δ_2^2 are the squared complex wavenumbers of the two compressional waves, and are given by

$$\delta_1^2 = \frac{\omega^2}{2(PR-Q^2)}\left[P\tilde{\rho}_{22} + R\tilde{\rho}_{11} - 2Q\tilde{\rho}_{12} - \sqrt{\Delta}\right] \tag{35a}$$

$$\delta_2^2 = \frac{\omega^2}{2(PR-Q^2)}\left[P\tilde{\rho}_{22} + R\tilde{\rho}_{11} - 2Q\tilde{\rho}_{12} + \sqrt{\Delta}\right] \tag{35b}$$

where

$$\Delta = \left(P\tilde{\rho}_{22} + R\tilde{\rho}_{11} - 2Q\tilde{\rho}_{12}\right)^2 - 4\left(PR-Q^2\right)\left(\tilde{\rho}_{11}\tilde{\rho}_{22} - \tilde{\rho}_{12}^2\right) \tag{36}$$

The chosen determination of the square root in equations (35a) and (35b) is the one with the positive real part. The two eigenvectors can be written

$$[\Phi_1] = \begin{bmatrix} \Phi_1^s \\ \Phi_1^f \end{bmatrix}, \qquad [\Phi_2] = \begin{bmatrix} \Phi_2^s \\ \Phi_2^f \end{bmatrix} \tag{37}$$

By employing equation (29), the following equation gives the ratio of the velocity of the frame over the velocity of the air for the two compressional waves and indicates what medium the waves propagate in preferentially

$$\mu_i = \frac{P\delta_i^2 - \omega^2\tilde{\rho}_{11}}{\omega^2\tilde{\rho}_{12} - Q\delta_i^2} \qquad i = 1,2 \tag{38}$$

Four characteristic impedances can be defined since both wave simultaneously propagate in the air and the frame of the porous material. The characteristic impedance related to a wave propagating in the positive x direction in the air is denoted by

$$Z^f = \frac{p}{j\omega u_x^f} \tag{39}$$

Substituting equations (13b) in equation (39), the characteristic impedance related to the air can be rewritten as for the two compressional waves as

$$Z_i^f = \left(R + Q/\mu_i\right)\frac{\delta_i}{\phi\omega}, \qquad i = 1,2 \tag{40}$$

Similarly, the characteristic impedance related to a forward propagating wave in the solid is denoted by

$$Z^s = \frac{-\sigma_{xx}^s}{j\omega u_x^f} \tag{41}$$

Substituting equations (13a) in equation (41), the characteristic impedance related to the solid phase can be rewritten as for the two compressional waves as

$$Z_i^s = \left(P + Q\mu_i\right)\frac{\delta_i}{\omega}, \qquad i = 1,2 \tag{42}$$

4.5 The Shear Wave

As in the case for an elastic solid, the wave equation for the rotational wave can be obtained by using vector potentials. Two vector potentials, Ψ_s and Ψ_f, for the frame and for the air, are defined as follows:

$$u = \nabla \times \Psi^s \tag{43a}$$

$$U = \nabla \times \Psi^f \tag{43b}$$

Substitution of the displacement representation, equations (43a) and (43b), into equations (26a) and (26b) yields

$$-\omega^2\left(\tilde{\rho}_{11}\Psi^s + \tilde{\rho}_{12}\Psi^f\right) = N\nabla^2\Psi^s \tag{44a}$$

$$-\omega^2\left(\tilde{\rho}_{12}\Psi^s + \tilde{\rho}_{22}\Psi^f\right) = 0 \tag{44b}$$

The wave equation is denoted by

$$\nabla^2\Psi + \frac{\omega^2}{N}\left(\frac{\tilde{\rho}_{11}\tilde{\rho}_{11} - \tilde{\rho}_{12}^2}{\tilde{\rho}_{11}}\right)\Psi = 0 \tag{45}$$

The squared wavenumber for the shear wave is defined as

$$\delta_3^2 = \frac{\omega^2}{N}\left(\frac{\tilde{\rho}_{11}\tilde{\rho}_{22} - \tilde{\rho}_{12}^2}{\tilde{\rho}_{22}}\right) \tag{46}$$

and the ratio of amplitudes of the displacement of the air and the fluid is given by

$$\mu_3 = \frac{-\tilde{\rho}_{12}}{\tilde{\rho}_{22}} \tag{47}$$

Employing the three Biot wavenumbers and the coupling coefficients we can use the traveling wave approach to establish the displacements within the foam. This analytical approach will be demonstrated after a more in depth study of these wavenumbers and their physical characteristics is presented.

4.6 The Three Biot Waves in Air-Saturated Acoustic Foam

The following discussion concerning the wave velocities and attenuation coefficients of the three wave types common to porous media will be in the context of partially reticulated acoustic foam, an integral part of this study. The material properties for a typical partially reticulated acoustic foam is listed in Table 4.3. In this case, a strong coupling exists between the fluid and the frame of the porous layer. The two compressional waves exhibit very different properties and are identified as the fast wave, or P1 wave, and the slow wave, or P2 wave. These waves correspond to classic compressional waves. In the absence of the fluid, only one compressional wave exists. The shear wave, sometimes referred to as the S wave, propagates within the frame of the porous media since fluid does not support shear [40]. The foundation for these distinctions are due to the fact that the ratio μ of the velocities of the fluid and the frame is close to 1 for the fast wave, while these velocities are nearly opposite for the slow wave. Also, the damping due to viscosity is much stronger for the slow wave relative to the fast wave. (The characteristic dimensions for partially reticulated polyurethane foam are $\Lambda = 28x10^{-6}$ and $\Lambda' = 320x10^{-6}$).

Table 4.3: Typical properties of partially-reticulated acoustic foam.

Properties of Partially-reticulated foam	
Flow Resistivity, σ (Ns/m)	25.0×10^3
Porosity, ϕ	0.90
Tortuosity, ε'	7.8
Poisson's ratio, ν	0.4
Shear modulus, N (N/m^2)	286×10^3
Loss factor, η	0.265
Solid mass density, ρ_s	30.0
Fluid mass density, ρ_f	1.213

Consider the case of forward propagating acoustic wave and adopting an $\exp(j\omega t - k\tilde{r})$ sign convention, the complex wavenumber can be defined as $k = \beta - j\alpha$, where β is the phase constant, α is the attenuation coefficient, and both parameters have a positive real part. The real part is related to the velocity of the wave which is given by $c = \omega/\beta$. The wave speed can be expressed in non-dimensional form by normalizing the value with respect to the speed of sound in air under standard conditions. Recall that wavelength is defined as $\lambda = 2\pi/\beta$. The attenuation can be described in dimensionless form as $\alpha\lambda = 2\pi\alpha/\beta$, which represents the attenuation per wavelength.

The normalized wave speeds for the three wave types propagating in partially reticulated foam, using the material properties of Table 4.2, are plotted in Figure 4.3(a) as a function of frequency. Observing the P1 wave, it appears that it's speed is virtually independent of frequency. It has a value of approximately 0.731 or 250.69 m/s. An important conclusion can be drawn concerning the P1 wave when it's speed is compared to that of a compressional wave traveling in the equivalent homogeneous elastic medium. The phase speed of the equivalent homogeneous elastic medium is given by $c = \sqrt{P/\rho_1}$ or 239.27 m/s. Note that P, represents the elasticity coefficient of the frame in a vacuum and is defined by equation (30) and ρ_1 is the density of the material that constitutes the solid phase. It can be concluded that the P1 wave corresponds to the frame wave. Note that the presence of the fluid in the pores of the materials increases the stiffness of the bulk material. Consequently, the frame wave in the elastic porous material is faster than

the corresponding wave in a homogeneous elastic material possessing the same bulk modulus as the *in vacuo* porous material.

In Figure 4.3(a), the P2 wave exhibits very different behavior when compared to the P1 wave. It increases from a very small value in the low frequency region and approaches an asymptotic limit of 0.3212 or 110.17 m/s in the high frequency region. The asymptotic limit of the phase speed for the porous material with a rigid frame is determined by $c = \sqrt{R/\tilde{\rho}_{22}}$, and this value is 113.85 m/s. Note that R describes the elasticity coefficient of the fluid phase, defined by equation (16), and $\tilde{\rho}_{22}$ is the mass coefficient of the fluid phase defined in equation (28). This limiting value depends on the inertial parameter known as the tortuosity [32]. It is evident that the P2 wave corresponds to the airborne wave due to it's similarity to the wave that propagates in a fluid component of a rigid porous medium. In the present case, the finite frame elasticity has the effect of reducing the phase velocity of the airborne wave below the value it would have in an equivalent rigid porous material.

The phase speed of the shear wave or P3 wave in the foam is practically independent of frequency, as shown in Figure 4.3(a), is equal to 0.287 or 98.56 m/s. The shear wave speed in the homogeneous elastic medium is described by $c = \sqrt{N/\rho_1}$ or 97.64 m/s. This observation supports the fact that the shear wave is strictly a frame wave since fluids do not undergo shearing effects. Considering the three possible wave-types common to partially-reticulated acoustic foam, the frame wave is the faster of the three waves. Unlike other porous materials such as glass wool, the coupling of the solid and fluid phase motion cannot be neglected in acoustic foams.

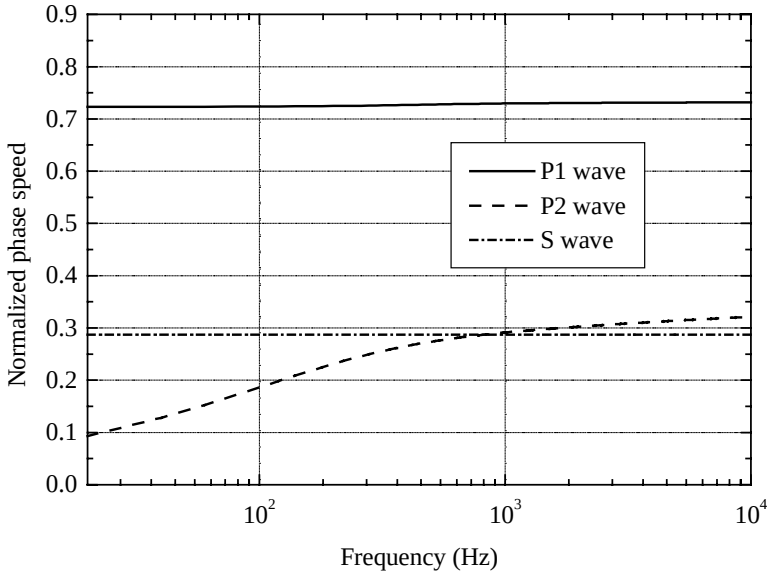

Figure 4.3(a): Variation of the normalized phase speed of the P1, P2 and S waves propagating in acoustic foam with respect to frequency.

The attenuation per wavelength for the three wave-types is plotted in Figure 4.3(b) as a function of frequency. Recall that this quantity is dimensionless and is described by $\alpha\lambda = 2\pi\alpha/\beta$. The attenuation per wavelength of the frame wave (or P1 wave) and the shear wave (or P3 wave) exhibit little frequency dependence possessing approximate values of 0.7618 and 0.8205, respectively. In contrast the attenuation per wavelength of the airborne wave (or P2 wave) decreases monotonically from large values at low frequencies. It becomes smaller than the other values above 4000 Hz In the low frequency region The airborne wave is the most heavily damped among the three wavetypes. Accordingly, any foam lined noise control treatment in which the major portion of the acoustical energy is carried through the lining by the airborne wave can be expected to give good performance since a relatively large amount of energy will be dissipated as the wave travels through the foam. These observations related to the wave speeds and attenuation coefficients have also been predicted by other theoretical models based on the Biot theory concerning wave propagation in acoustic foams [74].

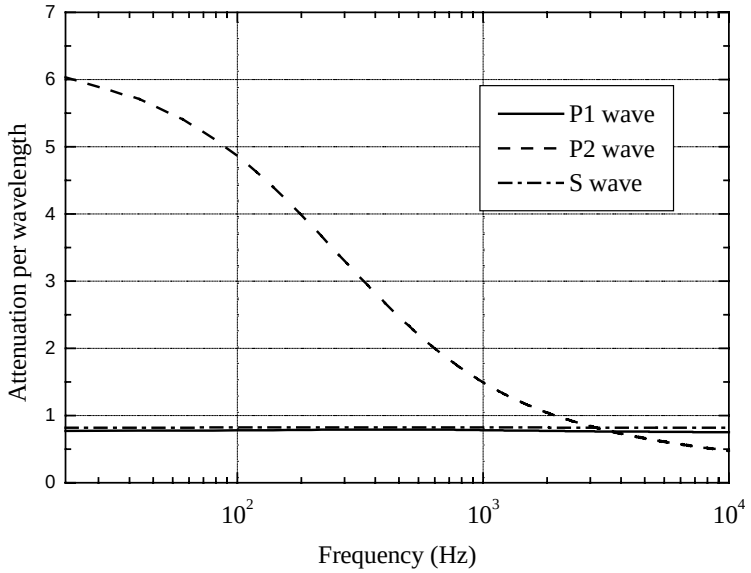

Figure 4.3(b): Variation of the attenuation coefficient of the P1, P2 and S waves propagating in acoustic foam with respect to frequency.

4.7 Example Application: Prediction of Surface Impedance at Normal Incidence for a Layer of Porous Material Backed by a Rigid Wall

A 2.0 cm layer of partially-reticulated acoustic foam excited by a unit amplitude plane wave propagating at normal incidence to the front surface of the material is shown in Figure 4.4. The porous layer is considered to be bonded to an impervious wall at it's rear surface and is infinite in the longitudinal direction. In this normal acoustic field, the shear wave is not excited and only the two compressional waves propagate in the material. The behavior of the material under these conditions is studied by evaluating the variation of the surface impedance relative to the excitation frequency. The foundation for this analysis is based on the derivation presented in section 4.4, and standard atmospheric conditions are assumed (i.e. density of air, ρ_o =1.213 kg/m^3 and the speed of sound in air, c_o=343 m/s).

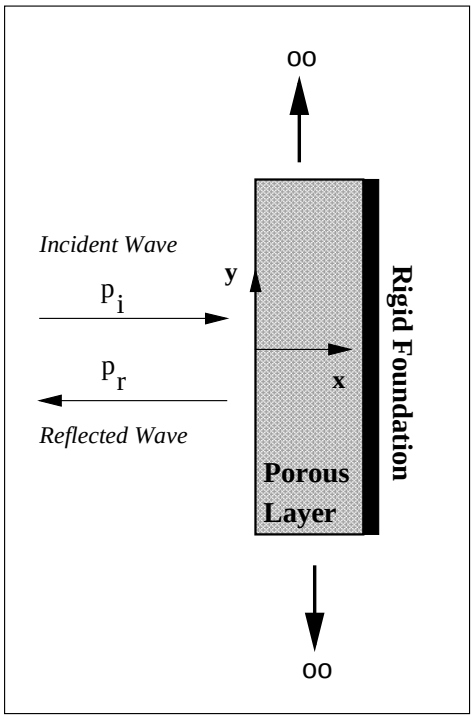

Figure 4.4 Illustration of a porous layer bonded to a rigid foundation and excited by a normal incident plane acoustic wave.

Using a frequency domain, traveling wave approach, where the $e^{j\omega t}$ time dependence is suppressed, the total acoustic pressure near the front surface of the material is described by

$$p = \exp(-k_o x) + R\{\exp(k_o x)\} \tag{48}$$

where $k_o = \omega / c_o$ is the acoustic wavenumber. The symbol R denotes the amplitude of the reflected wave at the front surface of the material. Employing the equation of linear momentum [75] and equation (48), one may determine the velocity of the acoustic field at the front surface of the porous layer as

$$\dot{u}^a = \frac{1}{\rho_o c_o}\left(\exp(-k_o x) - R\{\exp(k_o x)\}\right) \tag{49}$$

The velocity of the frame and the air in the material are, respectively

$$\dot{u}^s = V_1^i \exp(-j\delta_1 x) + V_1^r \exp(j\delta_1 x) + V_2^i \exp(-j\delta_2 x) + V_2^r \exp(j\delta_2 x) \tag{50}$$

and

$$\dot{u}^s = \mu_1\left[V_1^i \exp(-j\delta_1 x) + V_1^r \exp(j\delta_1 x)\right] + \mu_2\left[V_2^i \exp(-j\delta_2 x) + V_2^r \exp(j\delta_2 x)\right] \tag{51}$$

The wavenumbers δ_1 and δ_2 are defined in equations (35), and μ_1 and μ_2 by equations (38). The quantities V_i^1 and V_r^1 are the velocities of the frame at x=0 associated with the incident and reflected P1 wave. Similarly, the quantities V_i^2 and V_r^2 are the velocities of the frame at x=0 associated with the incident and reflected P2 wave. The stresses in the solid and fluid phase of the material are given by

$$\sigma_{xx}^s = -Z_1^s\left[V_1^i \exp(-j\delta_1 x) - V_1^r \exp(j\delta_1 x)\right] - Z_2^s\left[V_2^i \exp(-j\delta_2 x) - V_2^r \exp(j\delta_2 x)\right] \quad (52)$$

and

$$\sigma_{xx}^s = -\phi Z_1^s \mu_1\left[V_1^i \exp(-j\delta_1 x) - V_1^r \exp(j\delta_1 x)\right] - \phi Z_2^s \mu_2\left[V_2^i \exp(-j\delta_2 x) - V_2^r \exp(j\delta_2 x)\right] \quad (53)$$

The unknown wave amplitudes can be evaluated by enforcing the boundary conditions which ensure continuity of pressure and continuity of velocity at the front surface of the material and set the velocities equal to zero at the porous material-wall interface. These boundary conditions are :

$$x = 0 \quad \begin{cases} \sigma_{xx}^s = -(1-\phi)p \\ \sigma_{xx}^f = -\phi p \\ \phi \dot{u}^f + (1-\phi)\dot{u}^s = \dot{u}^a \end{cases} \quad (54)$$

$$x = L \quad \begin{cases} \dot{u}^s = 0 \\ \dot{u}^f = 0 \end{cases}$$

Applying these five boundary conditions, the unknown wave amplitudes representing the reflected wave in the air (R) and the four incident and reflected waves associated with the porous layer $\left(V_1^i, V_1^r, V_2^i, V_2^r\right)$ can be determined. Once these wave amplitudes are established, the surface impedance can be calculated using

$$Z = \frac{p(x=0)}{\dot{u}^a(x=0)} \quad (55)$$

It is interesting to compare the surface impedance exhibited by the glass wool termed ‘Domisol Coffrage’ and partially-reticulated acoustic foam; two different air-

saturated porous materials. The glass wool properties are summarized in the Table 4.2. The characteristic dimension values for glass wool are $\Lambda = 0.56x10^{-4}$ and $\Lambda' = 1.12x10^{-4}$. The normalized surface impedance for a slab of the glass wool is plotted in Figure 4.5(a) as a function of frequency up to 2000 Hz. A secondary set of curves representing the prediction of the impedance of a similar material with a rigid frame are also plotted. (This plot shows excellent agreement with the one presented by Allard [19] for the same material). The frame resonance occurs when the real part of the impedance reaches a minimum at 821.3 Hz. The normalized surface impedance for a layer of partially-reticulated acoustic foam is plotted in Figure 4.5(b) as a function of frequency up to 2000 Hz. A secondary set of curves representing the prediction of the impedance of a similar material with a rigid frame are also plotted. The frame of acoustic foam is lighter and less stiff than that of glass wool, and this creates a stronger coupling between the solid and fluid phase of the material. This characteristic is evident in Figure 4.5(b) which shows that the frame wave cannot be ignored over the entire frequency range.

Table 4.2: Typical properties of glass wool.

Properties of Glass Wool 'Domisol Coffrage'	
Flow Resistivity, σ (Ns/m)	$40.0x10^3$
Porosity, ϕ	0.94
Tortuosity, ε'	1.06
Poisson's ratio, ν	0.0
Shear modulus, N (N/m^2)	$220.0x10^4$
Loss factor, η	0.1
Solid mass density, ρ_s (kg/m^3)	130.0
Fluid mass density, ρ_f (kg/m^3)	1.213

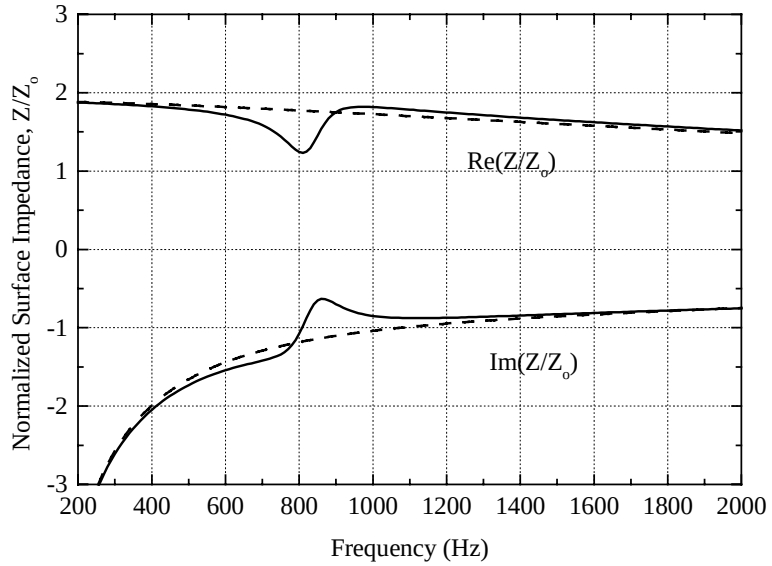

Figure 4.5(a): Normalized surface impedance vs. frequency of Glass wool. The thickness of the layer is 5.6 cm. Normalized impedance of glass wool: ——. Normalized impedance of similar rigid framed material: - - - - - -.

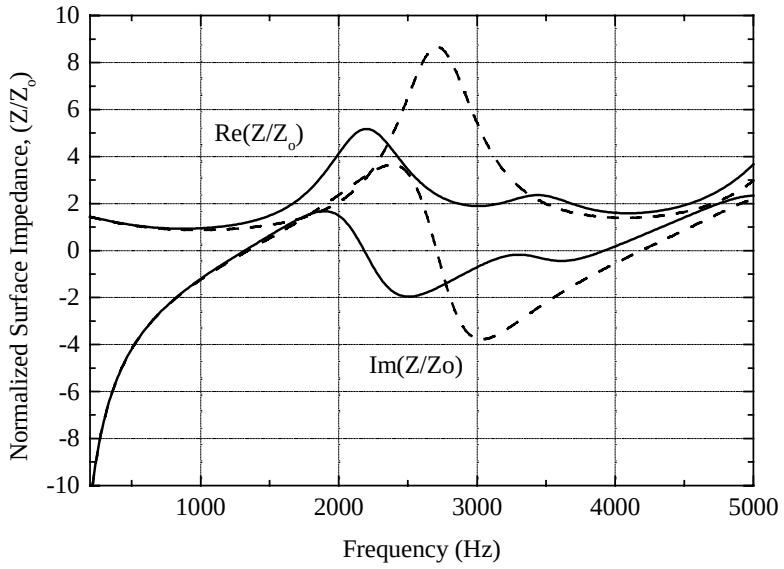

Figure 4.5(b): Normalized surface impedance vs. frequency of acoustic foam. The thickness of the layer is 2.0 cm. Normalized impedance of acoustic foam: ——. Normalized impedance of similar rigid framed material: - - - - - -.

4.8 The Finite Element Method

The finite element method is a numerical procedure for analyzing structures and continuum when the problem is too complicated to be solved satisfactorily by classical analytical methods. The basic concept of the finite element method is *discretization* or modeling a continuum as an assemblage of small parts or elements. Each element is of a simple geometry and therefore is much easier to analyze than the actual structure. In essence, a complicated solution may be approximated by a model that consists of piecewise continuous simple solutions. The body analyzed can have arbitrary shape, loads and support conditions. The mesh can mix elements of different types, shapes, and physical properties. Another attractive feature of the finite element method (FEM) is the close physical resemblance between the actual structure and its finite element model. The model is not simply an abstraction. It is for these reasons that the finite element method is chosen to analyze smart foam, which is a composite poroelastic-piezoelectric system operating in an acoustic environment.

The finite element smart foam model is a linear approach which allows some assessment of linearity of the actual system when comparing the model predictions with experimental measurements. Furthermore, the finite element approach can be used to optimize the smart foam configuration with a reasonable degree of confidence and establish an active noise control simulation with smart foams.

Figure 4.7 illustrates a two-dimensional finite element model of a smart foam actuator enclosed in an air-filled duct. It is assumed that the walls of the duct are rigid and the actuator is excited by a voltage which generates sound propagation within the duct. The goal is to discretize the system into a finite number of elements and determine the resulting foam displacement and sound pressure field in the enclosure. The macroscopic foam displacement field and acoustic pressure are interpolated from the nodal degrees of freedom of the elements through the use of a shape function matrix, [N]. For example, the macroscopic air pressure $\{p\}^e$ is defined as $\{p\}^e = [N]\{\bar{p}\}^e$ where $\{\bar{p}\}^e$ is a vector of the pressure at the nodes of the element. The acoustic foam and air cavity are discretized using linear triangular finite elements [76] as shown in Figure 4.6. Linear triangular elements are used because of their simplicity and the fact that the element shape function

provides interelement continuity of the displacement field and it's first derivative. Note that the acoustic elements that discretize the airspace are uniformly distributed however, the foam elements are non-uniformly distributed to account for the piezoelectric actuator. As shown in Figure 4.6, the curved piezoelectric actuator (identified by the red line) is approximated using a collection of plane truss elements [76] which account for axial deformation. The axial deformation simulates the piezoelectric effect that occurs under electrical excitation of the actuator.

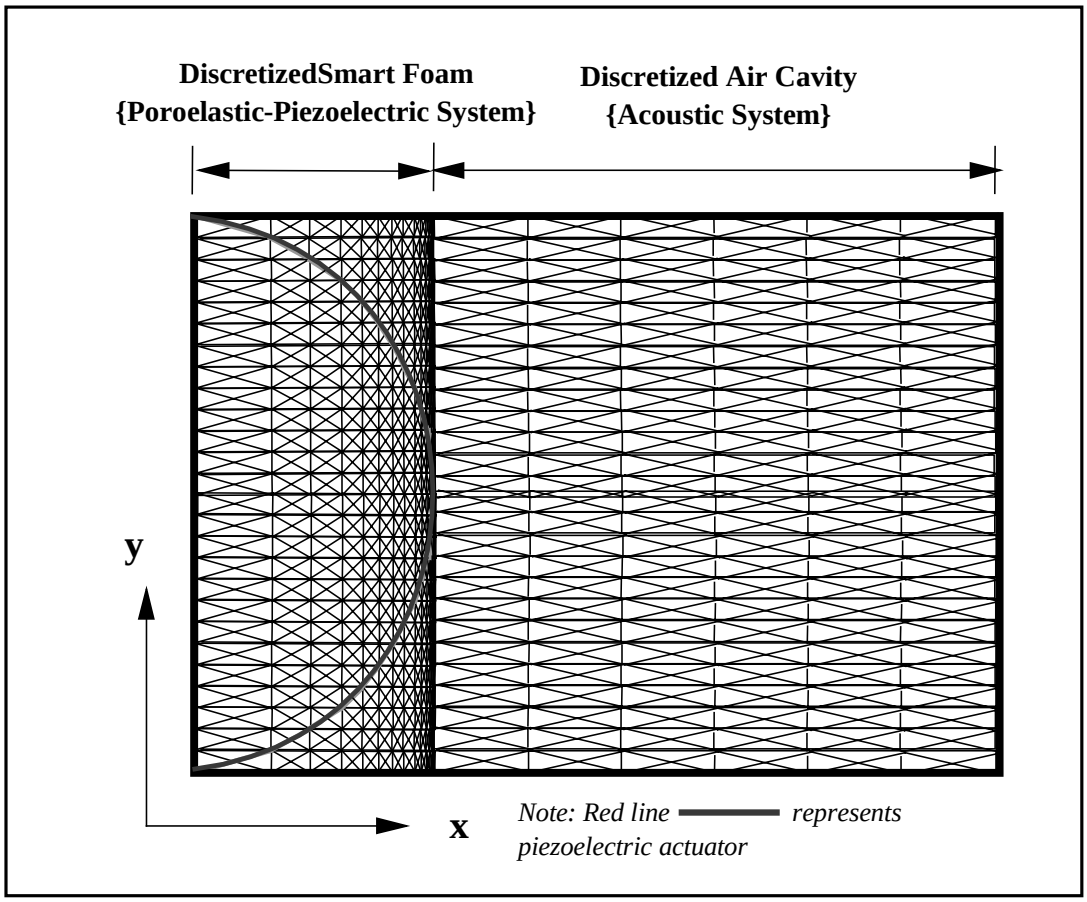

Figure 4.6. Illustration of *discretized* finite element model of smart foam in an air-filled duct.

The smart foam numerical model is programmed in MATLAB® by the author using the following steps:

(1) Mesh generation or dividing the system into finite elements, numbering the elements and corresponding nodes.

(2) Formulate the properties of each element by determining the nodal loads associated with all element deformation states.

(3) Assemble elements to determine the finite element model of the total system.

(4) Apply known applied loads or moments.

(5) Specify how the system is supported or set several nodal displacement to known values.

(6) Solve simultaneous linear algebraic equations to determine nodal degrees of freedom.

(7) Calculate element field variables from nodal degrees of freedom.

4.9 Finite Element Formulation for Poroelastic Media

In this section, a Lagrangian approach is combined with finite element discretization to obtain the discretized equations of motion for a poroelastic medium [59, 67]. For two-dimensional analysis, four degrees of freedom per node are used to define the displacement in the horizontal and vertical directions of each phase of the porous medium. The kinetic energy density for a poroelastic medium is defined as

$$dT = \frac{1}{2}\left\{\rho_{11}\left[\left(\dot{u}_x\right)^2 + \left(\dot{u}_y\right)^2\right] + 2\rho_{12}\left[\dot{u}_x\dot{U}_x + \dot{u}_y\dot{U}_y\right] + \rho_{22}\left[\left(\dot{U}_x\right)^2 + \left(\dot{U}_y\right)^2\right]\right\} \quad (56)$$

and the strain energy density is defined as

$$dV = \frac{1}{2}\left[\left\{\sigma_s\right\}^T\left\{\varepsilon_s\right\} + \left\{\sigma_f\right\}^T\left\{\varepsilon_f\right\}\right] \quad (57)$$

where the stress tensors in the solid and fluid phase are represented by

$$\left\{\sigma_s\right\} = \left[D_s\right]\left\{\varepsilon_s\right\} + \left[D_{sf}\right]\left\{\varepsilon_f\right\} \quad (58)$$

and

$$\{\sigma_f\} = [D_f]\{\varepsilon_f\} + [D_{sf}]\{\varepsilon_s\} \tag{59}$$

where $[D_s]$, $[D_f]$ and $[D_{sf}]$ denote the elasticity tensors related to the solid phase, the fluid phase and the strain coupling between both phases, respectively. These elasticity tensors can be written as

$$[D_s] = \begin{bmatrix} A+2N & A & 0 \\ A & A+2N & 0 \\ 0 & 0 & N \end{bmatrix} \tag{60}$$

and

$$[D_f] = R\begin{bmatrix} 1 & 1 & 0 \\ 1 & 1 & 0 \\ 0 & 0 & 0 \end{bmatrix} \tag{61}$$

and

$$[D_{sf}] = Q\begin{bmatrix} 1 & 1 & 0 \\ 1 & 1 & 0 \\ 0 & 0 & 0 \end{bmatrix} \tag{62}$$

The strain-displacement relations are

$$\{\varepsilon_s\} = [L]\{u\} \tag{63}$$

and

$$\{\varepsilon_f\} = [L]\{U\} \tag{64}$$

where

$$[L] = \begin{bmatrix} \partial/\partial x & 0 \\ 0 & \partial/\partial y \\ \partial/\partial y & \partial/\partial x \end{bmatrix} \tag{65}$$

Substituting equations (58)-(65) into equation (57) yields

$$dV = \frac{1}{2}\left(([L]\{u\})^T[D_s][L]\{u\} + 2([L]\{u\})^T[D_{sf}][L]\{U\} + ([L]\{U\})^T[D_f][L]\{U\}\right) \tag{66}$$

The dissipation energy is

$$D = \frac{1}{2}b\left\{\left(\dot{u}_x - \dot{U}_x\right)^2 + \left(\dot{u}_y - \dot{U}_y\right)^2\right\} \tag{67}$$

Defining an external surface force as $\{f\}=\{f_x \; f_y\}^T$, the work done per unit area by this surface force on the poroelastic layer is defined as

$$dW=(1-\phi)\{f\}^T\{u\}+\phi\{f\}^T\{U\} \tag{68}$$

Discretizing the poroelastic domain into classical linear triangular finite elements [35] and interpolating the macroscopic displacement fields, $\{u\}$ and $\{U\}$, in terms of the nodal displacement $\{\overline{u}\}$ and $\{\overline{U}\}$, yield for the e[th] element

$$\{u\}^e=\left[N_u\right]^{e^T}\{\overline{u}\}^e \tag{69}$$

and

$$\{u\}^e=\left[N_U\right]^{e^T}\{\overline{U}\}^e \tag{70}$$

By substituting equations (69)-(70) into (56),(66), and (67), the discretized energy densiies and work expressions are obtained. Next integrating over the domain of each element, summing the contribution from all elements and employing Lagrange's equations, the global discretized equations of motion are obtained

$$\left(-\omega^2\begin{bmatrix}[M_{ss}] & [M_{sf}]\\ [M_{sf}] & [M_{ff}]\end{bmatrix}+\begin{bmatrix}[K_{ss}] & [K_{sf}]\\ [K_{sf}] & [K_{ff}]\end{bmatrix}\right)\begin{Bmatrix}\overline{u}\\ \overline{U}\end{Bmatrix}=\begin{Bmatrix}F_s\\ F_f\end{Bmatrix} \tag{71}$$

Specifically, the components of equation (71) are defined as

$$\begin{aligned}
\left[M_{ss}\right]&=\sum_{e\in\Omega_e}\int_{\Omega_e}\left[N_u\right]_e\tilde{\rho}_{11}\left[N_u\right]_e^T dA\\
\left[M_{ff}\right]&=\sum_{e\in\Omega_e}\int_{\Omega_e}\left[N_U\right]_e\tilde{\rho}_{22}\left[N_U\right]_e^T dA\\
\left[M_{sf}\right]&=\sum_{e\in\Omega_e}\int_{\Omega_e}\left[N_u\right]_e\tilde{\rho}_{12}\left[N_U\right]_e^T dA\\
\left[K_{ss}\right]&=\sum_{e\in\Omega_e}\int_{\Omega_e}[L]\left[N_u\right]_e\left[D_s\right][L]\left[N_u\right]_e^T dA\\
\left[K_{ff}\right]&=\sum_{e\in\Omega_e}\int_{\Omega_e}[L]\left[N_U\right]_e\left[D_f\right][L]\left[N_U\right]_e^T dA\\
\left[K_{sf}\right]&=\sum_{e\in\Omega_e}\int_{\Omega_e}[L]\left[N_u\right]_e\left[D_{sf}\right][L]\left[N_U\right]_e^T dA
\end{aligned} \tag{72}$$

The force vectors are denoted by

$$\{F_s\} = (1-\phi)\sum_{e\in\Gamma}\int_{\Gamma_e}[N_u]_e\{F\}_e\,d\Gamma$$
$$\{F_f\} = \phi\sum_{e\in\Gamma}\int_{\Gamma_e}[N_U]_e\{F\}_e\,d\Gamma \qquad (73)$$

where $\{F\}_e$ are the applied forces.

4.9.1 Verification of Poroelastic Finite Element Model

The surface displacement of a layer of porous material resting on a rigid foundation and excited by a normal distributed force is studied to verify the poroelastic finite element model. The problem is illustrated in Figure 4.7 and is chosen because the results can be compared with the currently available solution based on the analytical Biot theory. The foam dimensions are 2.0 x 2.0 cm and the boundary conditions require zero displacement at x=L. The program establishes the horizontal motion of the liquid and solid phase in response to the forcing function of 1.0 N/m applied to the solid phase. A sample mesh is also shown in Figure 4.7. The displacement versus frequency for Domisol Coffrage and partially reticulated foam are shown in Figures 4.8 and Figure 4.9. Excellent agreement is achieved by using 11 elements (number of elements 0<x<L and y=0) in the direction of the forcing function. In the studied frequency range less than 1% error is observed between the two approaches.

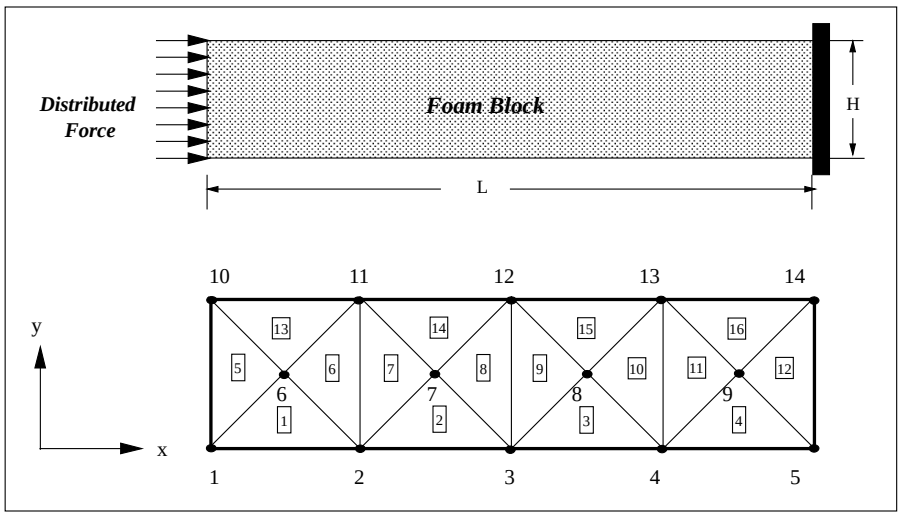

Figure 4.7: Illustration of a problem solved using numerical poroelastic model and sample finite element mesh of the system.

Observation of the surface displacement of the Glass Wool layer in response to a mechanical force illustrated in Figure 4.8 reveals that in the low frequency region (i.e. below 700 Hz), the displacement of each phase of the material increases with frequency. The solid phase exhibits higher displacement levels compared to the fluid phase showing that the fluid adds stiffness to the bulk material. A resonant frequency is encountered at approximately 910 Hz, and is related to the thickness of the material. It occurs at the frequency where the velocity is equal to zero at the foam wall interface and is a maximum at the foam surface (i.e. the foam thickness corresponds to $\lambda / 4$). Above 850 Hz, the response of the porous material begins to decrease and it is noted that each phase responds to the mechanical excitation with approximately the same displacement in this higher frequency region. Figure 4.9 illustrates the displacement of the layer of partially-reticulated foam corresponding to a mechanical force. Generally, the trends of the behavior of this material relative to the excitation frequency is similar to that of Glass Wool. However, some specific differences include a higher resonant frequency which occurs at approximately 1200 Hz and a “broader” resonance.

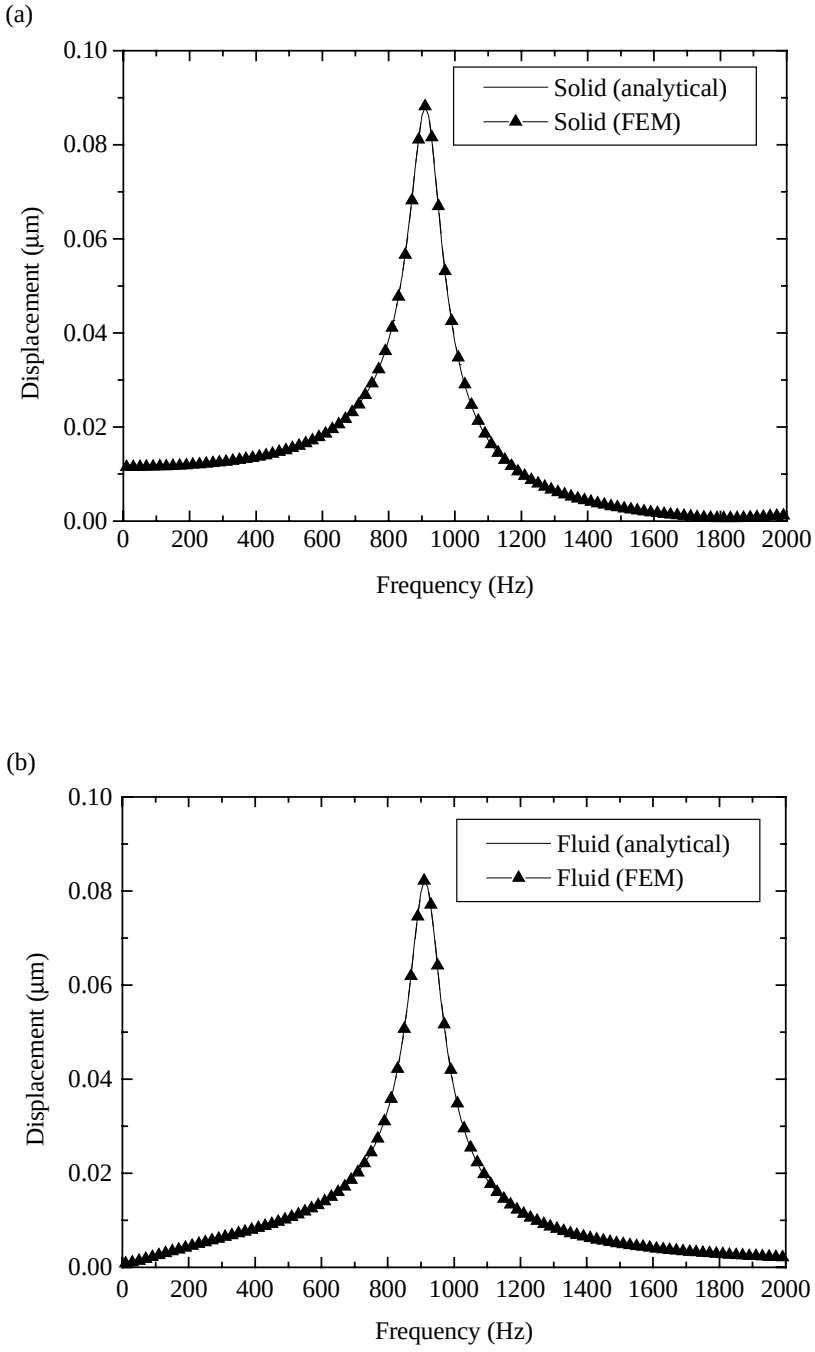

Figure 4.8: Surface displacement of Glass Wool due to mechanical force. A comparison of analytical and FEM results.

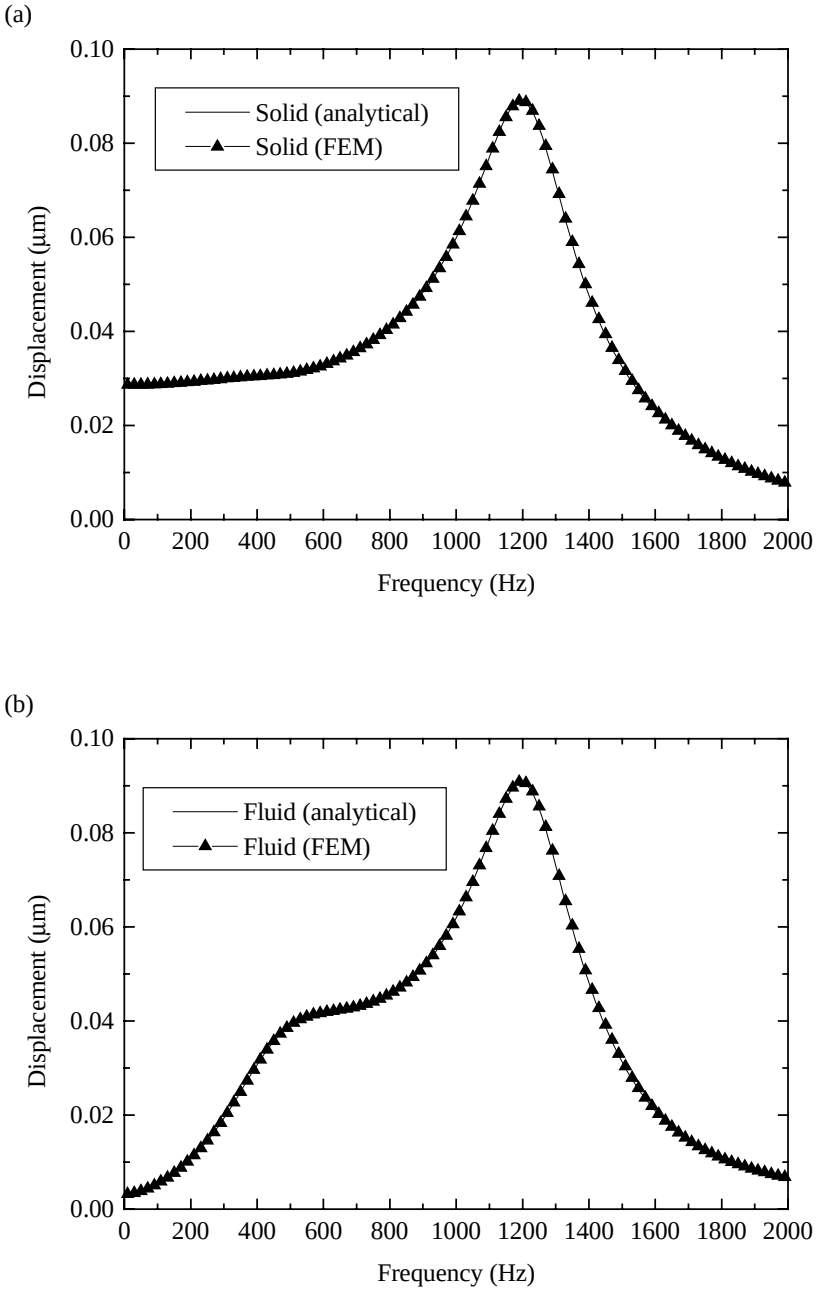

Figure 4.9: Surface displacement of partially-reticulated foam due to mechanical force. A comparison of analytical and FEM results

4.10 Finite Element Formulation for Ideal Fluids

The acoustical finite element formulation for an air-filled cavity is well known and established by Craggs [77]. As stated previously, in this analysis linear triangular elements are used to discretize the air space. It is stipulated that within each element, the variation of pressure P is prescribed by the nodal parameters associated with the nodes of the element. Therefore, the pressure for an acoustic element is determined by

$$\{P\} = [N]^T \{\overline{P}\}^e \tag{74}$$

The global acoustic system equation for an acoustic enclosure with an admittance A' on one boundary is given as

$$\left([T] - k^2[S] - j\rho\omega A'[C]\right)\{\overline{P}\} = \{Q\} \tag{75}$$

where $[T]$ denotes the kinetic energy matrix, $[S]$ represents the potential energy matrix and $[C]$ accounts for energy losses at the acoustic boundary. The vector {Q} accounts for the system forcing condition in terms of an input velocity. The various components of acoustic system equations of motion are defined as

$$[T] = \sum_{e\in\Omega_e} \int_{\Omega_e} [N][N]^T dA \tag{76}$$

$$[S] = \sum_{e\in\Omega_e} \int_{\Omega_e} [L][N]\left([L][N]^T\right) dA \tag{77}$$

where the differential operator is defined as

$$[L] = \begin{bmatrix} \partial/\partial x & 0 \\ 0 & \partial/\partial y \end{bmatrix} \tag{78}$$

The matrices corresponding to energy losses at the boundary and the forcing vector are expressed by

$$[C] = \sum_{e\in\Gamma_e} \int_{\Gamma_e} [N][N]^T d\Gamma \tag{79}$$

and

$$\{Q\} = -j\rho\omega \sum_{e\in\Gamma_e} \int_{\Gamma_e} [N]\{v\} d\Gamma \tag{80}$$

where the term {v} corresponds to the acoustic input velocity due to an excitation.

4.10.1 Verification of Acoustic Finite Element Model

Perhaps the most fundamental acoustic system is an air-filled duct excited by an oscillating piston. This problem has been addressed in many texts dealing with the introduction to acoustics. The accuracy of the two-dimensional acoustic finite element model presented in the previous section can be verified by comparing the results with analytical predictions of the sound pressure level within such a system. Note that the analytical solution describing the pressure fluctuations in a rigid air filled duct excited by an oscillating piston of velocity U is denoted by

$$p(x) = \frac{-j\rho_o c_o U \cos k(L-x)}{\sin(kL)} \tag{81a}$$

Use of the linear momentum equation enables the particle velocity distribution in the duct to be determined as

$$u(x) = \frac{U \sin k(L-x)}{\sin(kL)} \tag{81b}$$

Also note that the specific acoustic impedance varies along the length of the duct and is given by

$$z(x) = \frac{p(x)}{u(x)} = -j\rho_o c_o \cot(k\{L-x\}) \tag{81c}$$

In this analysis, the duct size is 5.0 cm (height) x 25 cm (length) and the excitation is provided by a piston that oscillates with a unit amplitude velocity. The analysis determines the sound pressure level at x=0 and x=L as a function of frequency. This problem statement and a sample mesh showing the finite element discretization of the air column is shown in Figure 4.10 and indicates the node and element numbering scheme. The element numbers are the described by the boxed numbers and the nodal numbers are not boxed. Figures 4.11 and Figure 4.12 shows the results for a duct having a rigid termination and anechoic termination. Excellent agreement is obtained in each case. To achieve less than 1.0% error within the 0<f<2000 Hz frequency range, the numerical model used 25 elements in the horizontal direction (number of horizontal elements 0<x<L and y=0). Consequently, the accuracy of the acoustic finite element model is verified.

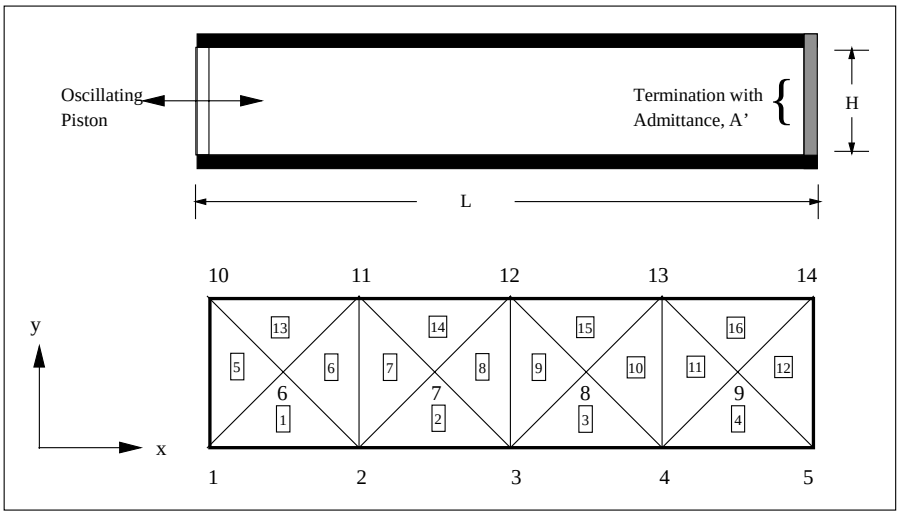

Figure 4.10: Illustration of a problem solved using numerical acoustic model and sample finite element mesh of the system.

Further observation of Figures 4.11 and equations (81) reveals that the resonance frequencies of the rigid duct occur at harmonic frequencies where sin(kL)=0, which according to equations (81a) and (81b) causes the complex pressure and particle velocity to become infinite. This infinite response of the acoustic pressure in the duct occur at frequencies such that $kL = n\pi$ where n is an integer. This corresponds to the relationship $f = nc/2L$, which are frequencies where an integer number of half wavelengths of sound can fit exactly inside the duct. Of course, in reality there is some dissipation in the system which will keep the response from becoming infinite. Note that the impedance is purely imaginary (i.e. it has only a reactive part and no resistive part) indicating that there is no net flow of energy. This is in contrast to the duct with an anechoic termination whose pressure fluctuation relative to excitation frequency is illustrated in Figure 4.12. In this case, the pressure is linearly related to the velocity by the characteristic acoustic impedance $\rho_o c_o$ which is a real quantity.

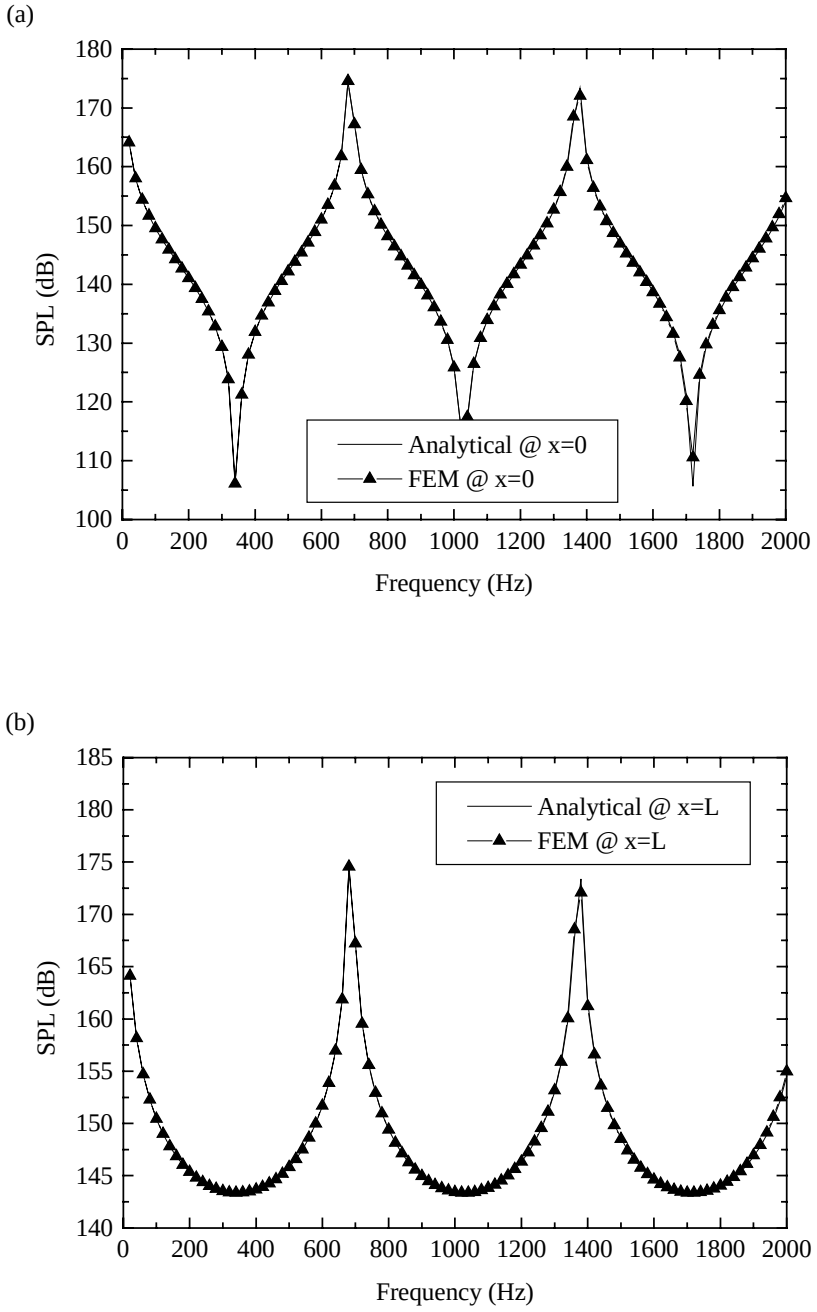

Figure 4.11: Verification of FEM model of acoustic system. Average SPL at x=0 and x=L vs. frequency for rigid air-filled duct excited by an oscillating piston.

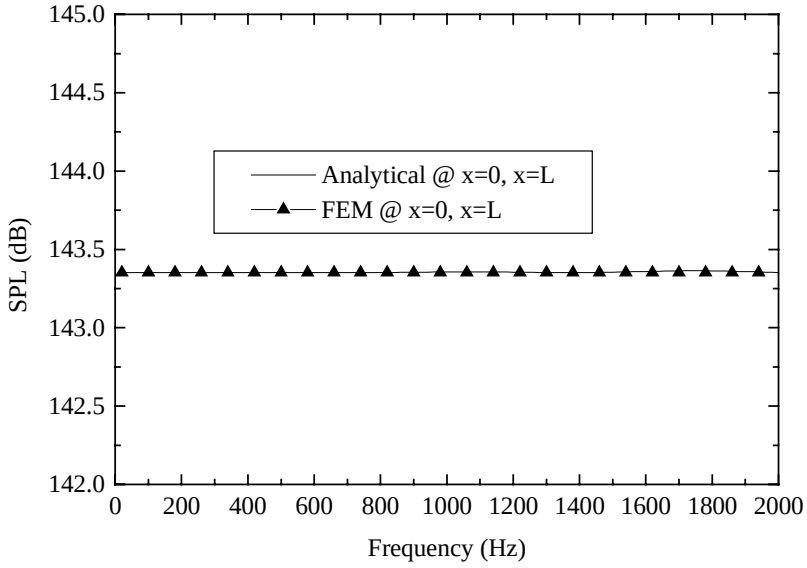

Figure 4.12: Verification of FEM model of acoustic system. Average SPL at x=0 and x=L vs. frequency for rigid air-filled duct with anechoic termination excited by an oscillating piston.

4.11 Finite Element Formulation of Piezoelectric Actuator

The piezoelectric effect is the coupled interaction between structural deformation and electrical fields in a material. Applying electrical fields to a piezoelectric material causes the material to strain and, conversely, applying mechanical strains causes electric fields to be generated in the piezoelectric material. In smart foam noise control applications, an electrical field is applied to the embedded piezoelectric actuator, known as PVDF, which is embedded in acoustic foam. To perform finite element analysis involving piezoelectric effects, coupled field elements which take into account structural and electrical coupling is needed. The PVDF actuator may be considered as an axial member of length L which experiences in-plane deformation as shown in Figure 4.13(a). Note that the element has one degree of freedom per node since only horizontal displacement is allowed. Figure 4.13(b) illustrates the same element but uses two degrees of freedom per node to do so. This is due to the change in orientation of the element as it is rotated by an angle, β, resulting in horizontal and vertical displacements at each node.

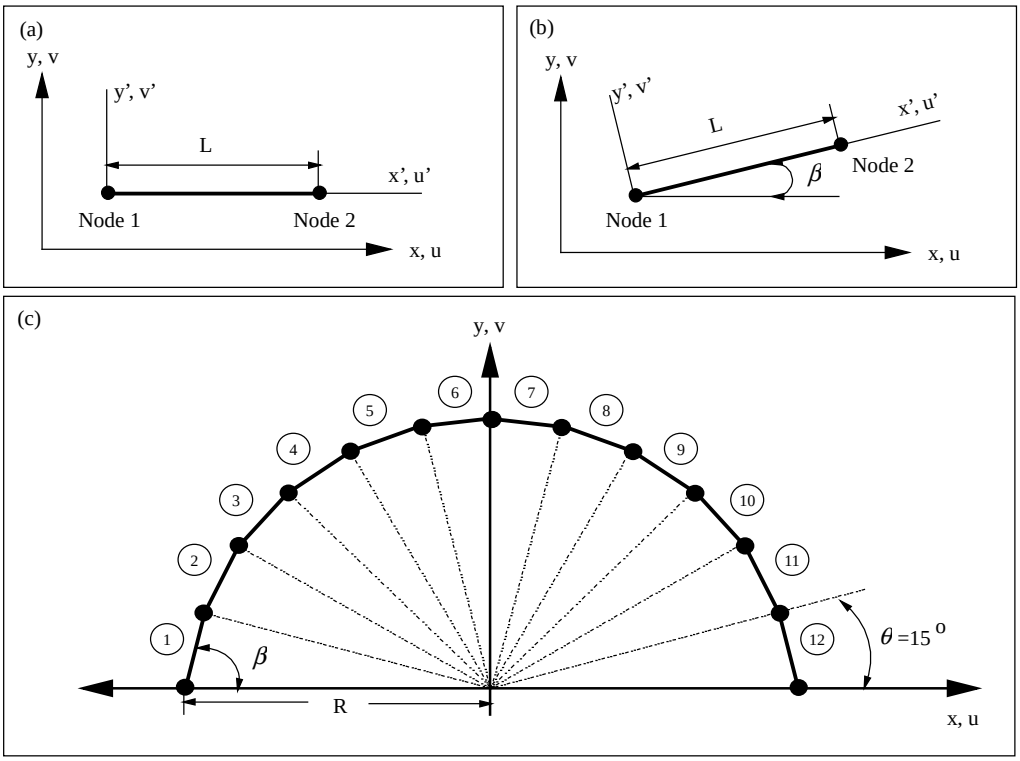

Figure 4.13(a): Piezoelectric finite element with one degree of freedom per node (b) Piezoelectric finite element with two degrees of freedom per node (c) Assembly of piezoelectric finite elements to establish cylindrical actuator of radius, R.

The kinetic energy density associated with axial deformation of the actuator is described by

$$dT = \frac{1}{2} m_L \dot{u}^2 \tag{81}$$

where m_L is the mass per unit length of the actuator and $\dot{u}$ denotes the axial velocity. The strain energy is expressed as

$$\begin{aligned} dV &= \frac{1}{2}\sigma\varepsilon + \frac{1}{2}\sigma d_{31} E \\ &= \frac{1}{2} Y \left(\frac{du}{dx}\right)^2 + \frac{1}{2}\left(Y\frac{du}{dx}\right)\left(d_{31}E\right) \end{aligned} \tag{82}$$

where the symbol Y is the young's modulus of the material, d_{31} is the piezoelectric strain constant, and E is the applied field represented by the ratio of the excitation voltage to the piezoelectric material thickness [29, 78]. The first term of the potential energy expression defined in equation (82) is associated with the mechanical strain and the

second term accounts for the piezoelectric effect. It will be seen that the second term is related to the forcing function of the system.

The piezoelectric material is discretized into classical plane truss finite elements [35] described by the shape functions $[N]^e = \begin{bmatrix} N_1 & N_2 \end{bmatrix}$. Interpolating the macroscopic displacement field, $\{u\}$, in terms of the nodal displacement $\{\bar{u}\}$ yield for the e[th] element

$$\{\bar{u}\}^e = [N]^{e^T} \{u\}^e \tag{83}$$

By substituting equation (83) into equations (81) and (82) , the discretized form of the energy densities for each element is obtained. Integrating over the e[th] element and making use of Lagrange's equations yields the discretized equations of motion for a single element as

$$\left(-\omega^2 [M] + [K]\right)\{\bar{u}\} = \{\bar{F}\} \tag{84}$$

Specifically, the components of equation (84) are

$$[M] = \int_{\Gamma_e} \rho [N]^e [N]^{e^T} d\Gamma \tag{85}$$

$$[K] = \int_{\Gamma_e} Y \frac{\partial}{\partial x}[N]^e \frac{\partial}{\partial x}[N]^{e^T} d\Gamma \tag{86}$$

The force vector is denoted by

$$\{F\} = Y d_{31} E \int_{\Gamma_e} \frac{\partial}{\partial x}[N]^e d\Gamma \tag{87}$$

A finite element model of the cylindrically-curved piezoelectric actuator is formed by assembling a collection of plane truss elements rotated by a specific angle from the horizontal position as described in Figure 4.13(c). There are four degrees of freedom associated with each piezoelectric element resulting from the horizontal and vertical motion of each node. This coordinate representation is more compatible with the poroelastic finite element model which account for four degrees of freedom for each phase of the material per node. Employing a transformation matrix, $[T]$, in the equations of motion yields

$$\left(-\omega^2 [T]^T [M][T] + [T]^T [K][T]\right)\{\bar{d}\} = [T]^T \{\bar{F}\} \tag{88}$$

where $\{\bar{d}\} = \{u_1\, v_1\, u_2\, v_2\}$ and accounts for the horizontal and vertical motion of each node as illustrated in Figure 4.14(b). The transformation matrix is defined as

$$T = \begin{bmatrix} \cos\beta & \sin\beta & 0 & 0 \\ 0 & 0 & \cos\beta & \sin\beta \end{bmatrix} \tag{89}$$

The global system representing the piezoelectric material is formulated by summing the contribution of all elements in the domain.

The established piezoelectric finite element model can now be used to simulate the vibrational response of a cylindrically-curved PVDF actuators as illustrated in Figure 4.13(c). Recall that the properties of the piezoelectric material used in this investigation are given in section 2.2. The following simulations establish the horizontal and vertical deflection of a PVDF actuator as the radius, R, is changed. Each actuator is excited with a 300 V_{rms} electrical input at 250 Hz. Figures 4.14 show the horizontal and vertical displacement over the range $-90^o \le \theta \le 90^o$ of three cylindrically-curved actuators of 0.5 inch, 1.0 inch and 2.0 inch radii, respectively. No constraints are enforced on the actuator boundaries and this is considered the "Free Case". These plots show that the horizontal and vertical displacement amplitudes increase as the radius of the actuator increases. A similar trend is observed in Figures 4.15 which represent the "Fixed Case" and enforces zero displacement at $\theta = -90^o$ and $\theta = 90^o$. Note that the actuator displacement converges to a steady state solution when approximately 10 elements per radial inch are used. This trend is valid up to an input frequency of 1000 Hz, which is the frequency range in which active control is performed during future experiments.

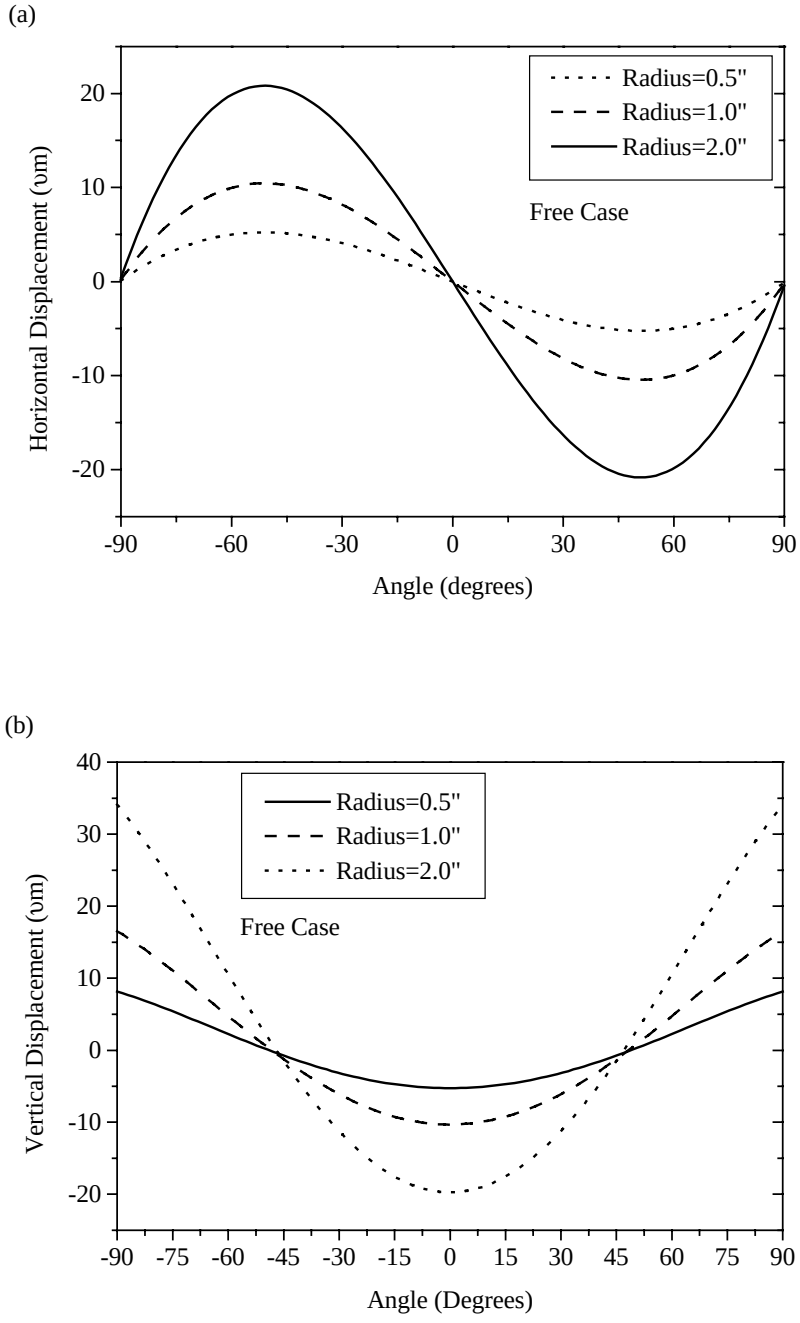

Figure 4.14(a): Horizontal displacement of PVDF actuator with "free" boundary conditions at 250 Hz with 300 V rms excitation. (b) Vertical displacement of PVDF actuator with "fixed" boundary conditions at 250 Hz with 300 V rms excitation.

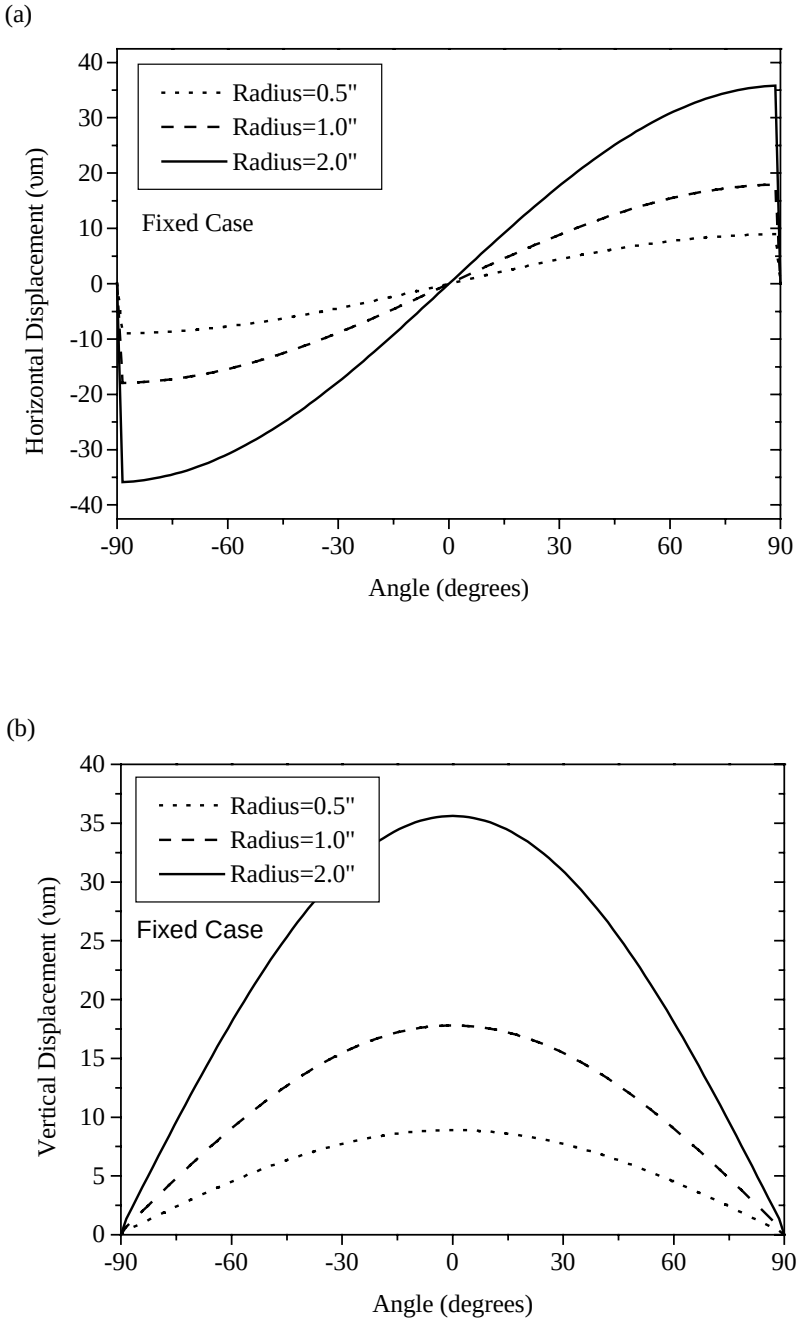

Figure 4.15(a): Horizontal displacement of PVDF actuator with "fixed" boundary conditions at 250 Hz with 300 V rms excitation. (b) Vertical displacement of PVDF actuator with "free" boundary conditions at 250 Hz with 300 V rms excitation.

The presented results concerning the numerical modeling of cylindrically-curved PVDF reveal that a fixed actuator exhibits the highest vertical displacement. With regard to radius, it is shown that the displacement of the actuator increases as the radius of the actuator increases. Figure 4.16 illustrates the average vertical displacement (in dB relative to 1 μm) for various cylindrically curved actuators. Each actuator has fixed end conditions and the input voltage is 300 V_{rms}. In Figure 4.16, the displacement is plotted as a function of frequency for an actuator with a 0.5, 1.0 and 2.0 inch radius. The results show that the resonance frequency denoted by the peak in each curve is in the very high frequency range (i.e. above 100 MHz). The frequency range of interest in this study is well below the first resonance frequency exhibited by each actuator. It is observed that in the low frequency region (i.e. below the first resonance), the larger actuator exhibits the highest displacement. Since the actuator displacement is directly proportional to sound output, the largest PVDF actuator is identified as the most acoustically efficient.

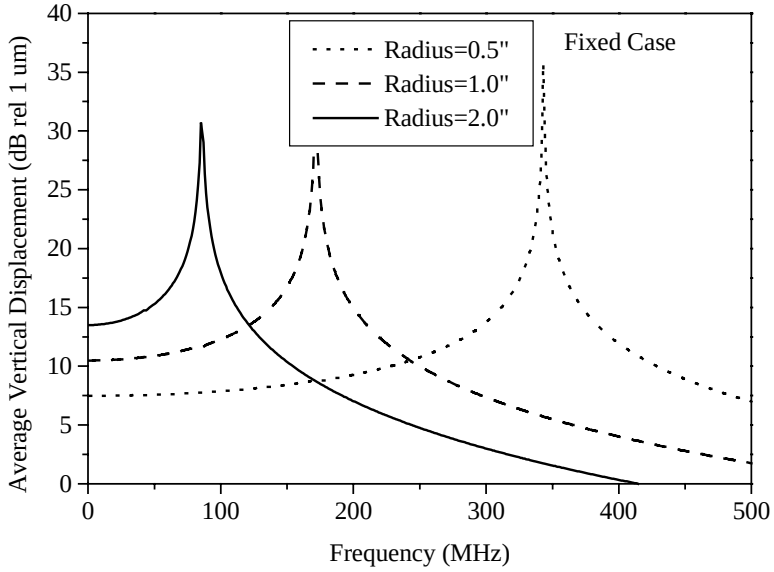

Figure 4.16: Average vertical displacement of PVDF actuator with "fixed" boundary conditions vs. frequency with 300 V rms excitation.

4.12 Coupling of Poroelastic Finite Elements with Acoustic Finite Element

In the development of a smart foam finite element formulation, the coupling conditions at the nodal points adjoining the different material interfaces must be enforced. The boundary conditions between the absorptive foam system, recognizing its' dual solid and fluid phases, and the acoustic system are

$$\begin{aligned} -\phi p &= \sigma_x^f \\ -(1-\phi)\, p &= \sigma_x^s \\ \sigma_{xy}^s &= 0 \\ v_x &= j\omega(1-\phi)u_x + j\omega\phi U_x \end{aligned} \tag{90}$$

Note that v_x denotes the velocity of the air in the acoustic system at the foam surface. The first two conditions of equation (90) enforce compatibility of normal forces in the air-fluid and air-solid interfaces, respectively. The third condition ensures that the shear force is equal to zero on the solid surface of the foam due to the assumed normal incident acoustic wave excitation. The fourth condition satisfies continuity of normal volume velocity at the interface.

Before establishing the coupled finite element formulation describing the poroelastic-acoustic system, some modification of the independent equations of motion for each subdomain must be made. Comparing equations (73) and (80), it is observed that the force vectors of the poroelastic and acoustic systems are expressed in different physical forms. The force vector is expressed in terms of forces for the poroelastic system while the force vector is expressed in terms of volume flow rates for the acoustic system. This mismatch arises because it is convenient to express the solution vector in terms of displacements for the foam system while the solution vector of the acoustic system is easily described in terms of acoustic pressure. Accordingly, it is necessary to collocate two nodes at the poroelastic-acoustic interface. One node is a component of the poroelastic finite element and the other node belongs to the acoustic finite element, allowing a decoupling of the two systems. The two subdomains are then coupled by enforcing the boundary conditions (90) in equations (73) and (80) to yield

$$
\begin{aligned}
F_i^1 &\approx (1-\phi)\sum_{j=1}^{m} p_j \int_{\Gamma_e} N_i N_j d\Gamma \\
F_i^2 &= 0 \\
F_i^3 &= \phi\sum_{j=1}^{m} p_j \int_{\Gamma_e} N_i N_j d\Gamma \\
F_i^4 &= 0 \\
Q_i &\approx \omega^2 \rho_o (1-\phi)\sum_{j=1}^{m} u_j \int_{\Gamma_e} N_i N_j d\Gamma + \omega^2 \rho_o \phi \sum_{j=1}^{m} U_j \int_{\Gamma_e} N_i N_j d\Gamma
\end{aligned}
\tag{91}
$$

The force vector of the poroelastic system is now described in terms of acoustic pressure and the force vector of the acoustic system is now described in terms of the displacements of the solid and fluid phases of the foam at the interface. As a result, the global finite element formulation of the poroelastic-acoustic system is denoted by

$$
\begin{bmatrix} [K_a] & [K_{af}] \\ [K_{af}^T] & [K_f] \end{bmatrix} \begin{Bmatrix} \{p\} \\ \{u\} \\ \{v\} \\ \{U\} \\ \{V\} \end{Bmatrix} = \begin{Bmatrix} \{Q\} \\ \{F^1\} \\ \{F^2\} \\ \{F^3\} \\ \{F^4\} \end{Bmatrix}
\tag{92}
$$

where the matrices $[K_a]$ and $[K_f]$ are the dynamic stiffness matrices for the independent acoustic and foam systems, respectively. The matrices $[K_{af}]$ and $[K_{af}^T]$ denotes the coupling between the acoustic and poroelastic subdomains and its' transpose, respectively. The sub-vector $\{Q\}$ on the right side accounts for any applied acoustic velocities. The sub-vectors $\{F^1\}$ and $\{F^2\}$ include any externally applied forces acting on the solid phase in the x and y directions, respectively. The sub-vectors $\{F^3\}$ and $\{F^4\}$ include any externally applied forces acting on the solid phase in the x and y directions, respectively.

4.12.1 Verification of Coupling of Poroelastic and Acoustic Finite Elements

Excellent analytical and numerical agreement has been obtained in the prediction of the surface displacement of a poroelastic layer and the acoustic pressure within a rigid-walled duct excited by a piston. The accuracy of the coupling method presented in the previous section can be established by determining the acoustic impedance and absorption coefficient of a foam sample placed at the termination of a rigid-walled duct as shown in Figure 4.17. An oscillating piston generates normal incident plane waves that impinge upon the foam sample whose properties are listed in Table 4.2. In the finite element analysis of the system, the total length of the duct, L_{xd}, and the length of the foam sample, L_{xf}, are 12.0 inches and 2.0 inches, respectively. There are 24 elements in the air in the horizontal direction and 10 elements in the foam in the horizontal direction. The height of the duct, L_{yd}, varies from 2.0 inches to 8.0 inches, while the number of elements in the vertical direction increase from 10 to 40 elements, respectively.

In Figures 4.18 and 4.19, the finite element results are compared to the analytical impedance and absorption coefficient solutions for a porous layer with a 2.0 inch thickness and infinite length in the vertical direction as a function of frequency. The graphs indicate that the impedance and the absorption coefficient determined by the finite element method approach the analytical solution as the height of the duct and the number of vertical elements are increased. Note that a duct height of 8.0 inches with 40 vertical elements yields the most accurate results in the frequency range studied. This observation implies that the stiffness offered by the horizontal constraints of the duct is minimized as the duct height increases, allowing convergence toward an infinite boundary solution.

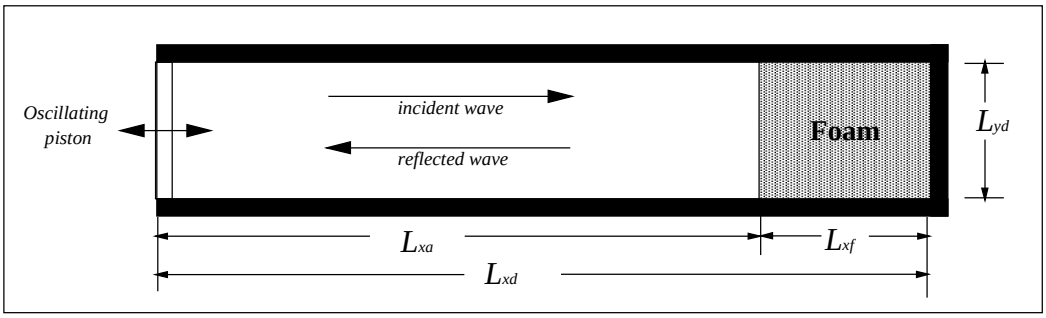

Figure 4.17: Illustration of acoustic waveguide terminated by a foam layer. Represents system used verify finite element acoustic-poroelastic coupling procedure.

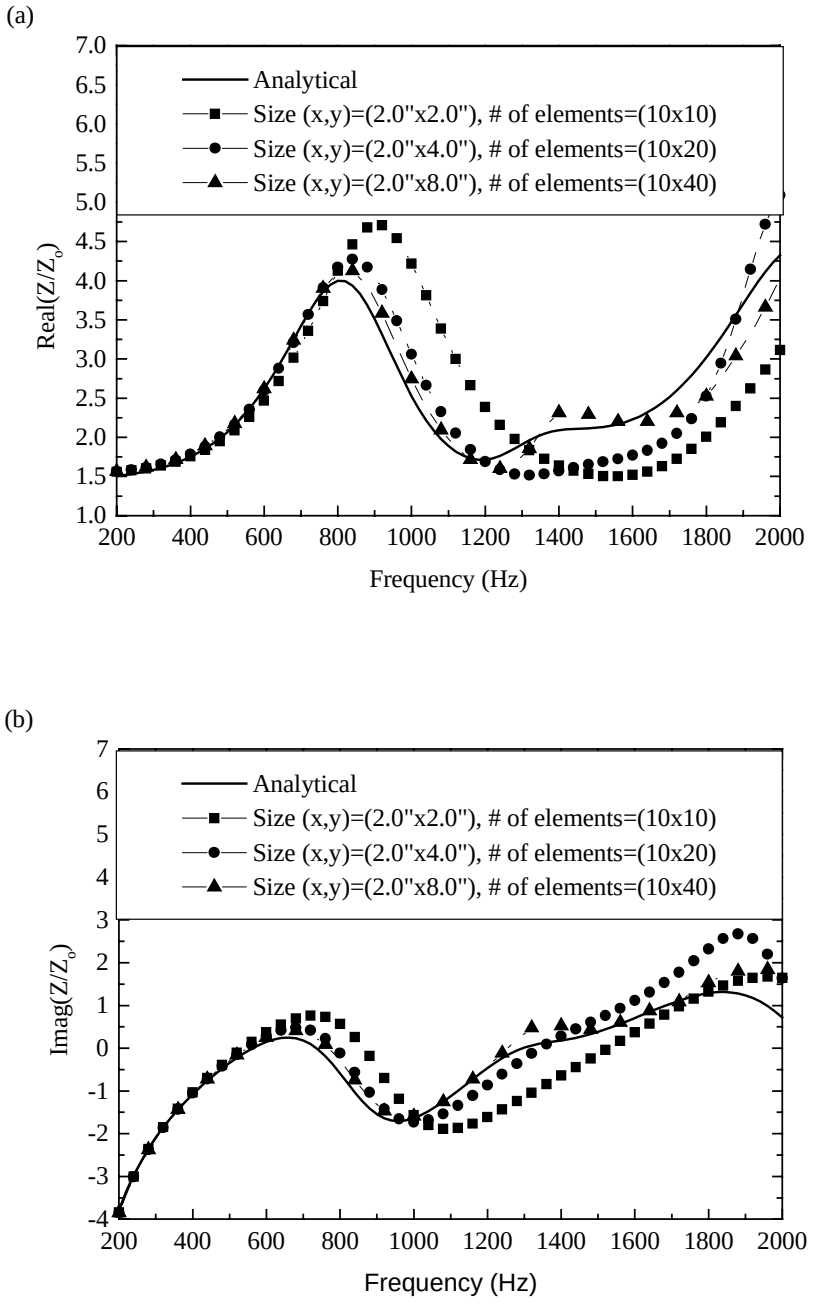

Figure 4.18: Comparison of normalized acoustic impedance as determined by analytical and finite element methods (a) Real part. (b) Imaginary part.

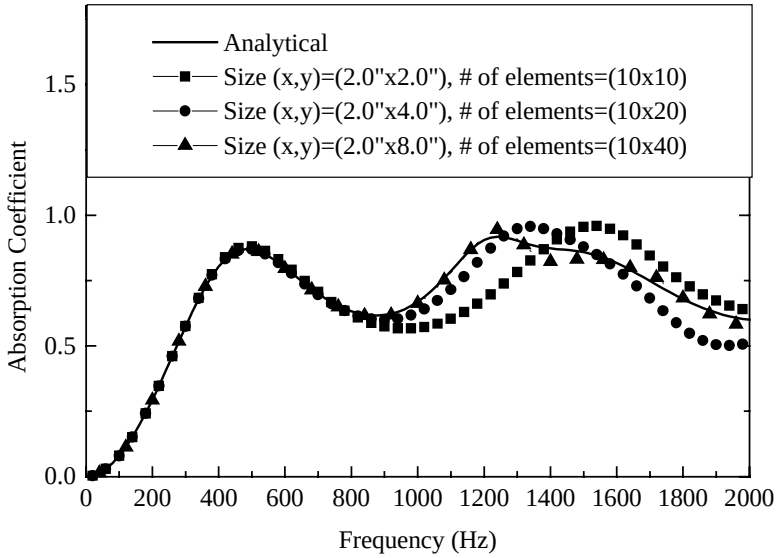

Figure 4.19: Comparison of normal incidence absorption coefficient as determined by analytical and finite element methods.

4.13 Coupling of the Poroelastic and Piezoelectric Finite Elements

Recall that the poroelastic and piezoelectric finite element models were constructed in terms of the nodal displacements of the elements. To enforce the boundary conditions at the poroelastic-piezoelectric actuator interface, one must require continuity of displacement. Accordingly, the nodal displacement associated with the actuator is equivalent to the nodal displacements describing the motion of the solid and fluid phase of the foam at the actuator foam interface.

4.14 Smart Foam Simulation by the Finite Element Method

The previously developed numerical formulations for the acoustic system, poroelastic system and piezoelectric actuator with the appropriate coupling conditions can now be combined to construct a complete smart foam actuator model. This model will now be used to identify the optimal smart foam configuration based on the maximum generated sound pressure level within the 100<f<1000 frequency range. This frequency range is investigated due to the demonstrated need for a PVDF configuration that exhibits good low frequency sound attenuation The setup for the simulation allows for the smart

foam actuator to be positioned within one end of a rigid duct that has an anechoic termination at the opposite end as shown in Figure 4.20. As stated earlier, the primary requirement for the smart foam to radiate sound is to contain a piezoelectric actuator that is physically curved in order to translate in-plane strain to out-of-plane motion with an applied voltage. With regard to this requirement, the sound output generated by "triangular" and "cylindrically" shaped actuators are studied. The height of the rigid duct and each smart foam array is 41.0 cm (16.0 inches) and the length of the air within the duct is approximately 1.0 m. The length of the smart foam array varies depending on the embedded PVDF configuration. A total of six unique smart foam configurations are investigated and each differ in physical orientation, wavelength, thickness and boundary conditions, as illustrated in Figure 4.20 and described below:

(1) *Four free triangles:* Array dimension (x,y)=(2.0 inches, 16.0 inch). PVDF actuator shaped as a series of four triangles with free rear boundary conditions.
(2) *Four free half-cylinders:* Array dimension (x,y)=(2.0 inches, 16.0 inch). PVDF actuator shaped as a series of four half-cylinders with free rear boundary conditions.
(3) *Eight free triangles:* Array dimension (x,y)=(1.0 inches, 16.0 inch). PVDF actuator shaped as a series of eight triangles with free rear boundary conditions.
(4) *Eight free half-cylinders:* Array dimension (x,y)=(1.0 inches, 16.0 inch). PVDF actuator shaped as a series of eight half-cylinders with free rear boundary conditions.
(5) *Four fixed triangles:* Array dimension (x,y)=(2.0 inches, 16.0 inch). PVDF actuator shaped as a series of four triangles with fixed rear boundary conditions.
(6) *Four fixed half-cylinders:* Array dimension (x,y)=(2.0 inches, 16.0 inch). PVDF actuator shaped as a series of four half-cylinders with fixed rear boundary conditions
(7) *Eight fixed triangles:* Array dimension (x,y)=(1.0 inches, 16.0 inch). PVDF actuator shaped as a series o eight triangles with fixed rear boundary conditions.
(8) *Eight fixed half-cylinders:* Array dimension (x,y)=(1.0 inches, 16.0 inch). PVDF actuator shaped as a series of eight half-cylinders with fixed rear boundary conditions

Figures 4.21 illustrates the sound pressure levels generated by each configuration at the anechoic termination. The responses of smart foam with various embedded PVDF actuators shaped as half-cylinders are presented in Figure 4.21(a). Similarly, the responses of smart foam with various embedded PVDF actuators configured as triangles are illustrated in Figure 4.19(b). In general, the primary observation seen in both figures is

that the sound generation of each smart foam configuration studied increases as the frequency of excitation increases. In Figure 4.21(a), it is further evident that the smart foam with cylindrically curved actuators having fixed boundary condition at the rear surface is the optimal configuration because it is the most acoustically efficient. By comparing the smart foam configured with four and eight half-cylinders, both having fixed boundary conditions, it is evident that the actuator with four half cylinders is the most efficient. These results confirm that for low frequency sound generation, as the size or wavelength of the embedded PVDF actuators increases an increase in sound output is yielded. Referring to Figure 4.21(a), a comparison of the response given by the cylindrically curved actuators with free boundary conditions at the rear surface indicates that below 400 Hz, they are capable of yielding comparable sound output as the fixed actuator cases. Above 400 Hz, it is revealed that as the size or wavelength of the free PVDF actuators is increased, they are capable of generating a higher sound output. However, in the studied frequency range, the smart foam with four embedded half-cylinders with fixed boundary conditions offers superior performance. Similar trends are noted in Figure 4.21(b), which reveal the response of various smart foam actuators configured with a series of embedded PVDF shaped as triangles. In comparison to the cylindrically-curved actuators, the triangular actuators are not as efficient. In summary, the smart foam actuators manufactured in Chapter 5 for the duct noise control experiments will contain cylindrically-curved PVDF with fixed boundary conditions. The radius of each actuator will be limited by the power amplifier specifications and the area of the commercially available PVDF film, but it is intended to allow the embedded PVDF to have the largest radius possible within the smart foam.

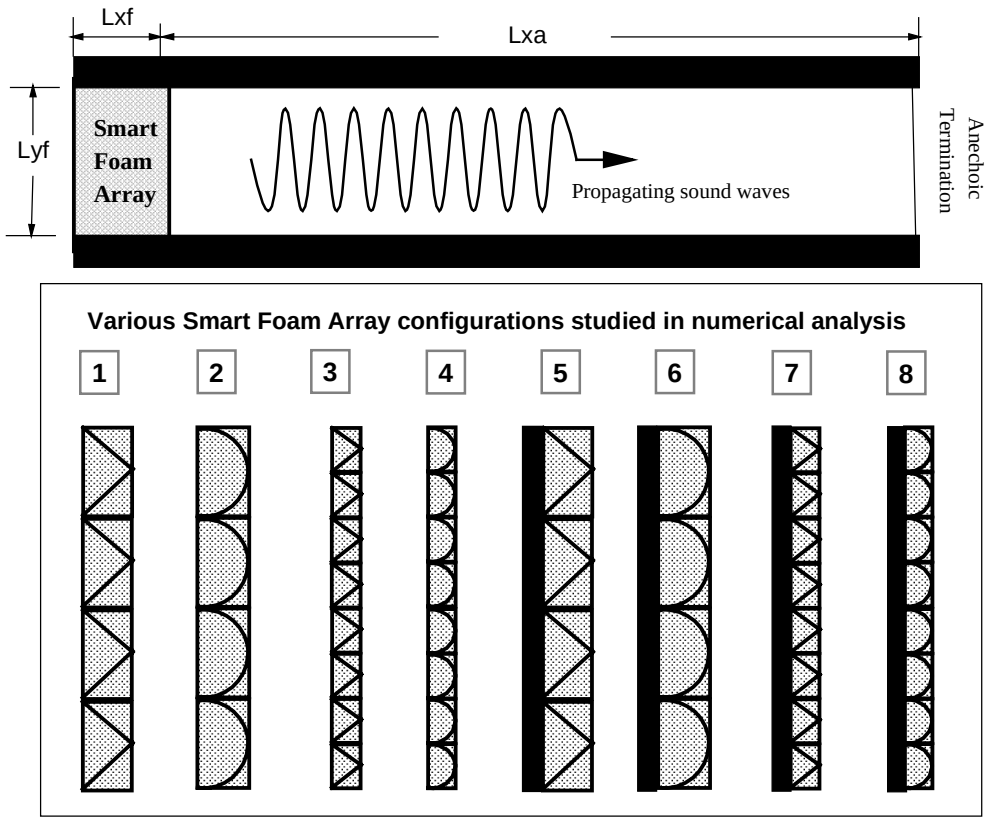

Figure 4.20 Illustration of smart foam actuator configurations investigated using the finite element approach : Smart foam with embedded PVDF shaped as (1) Four free triangles, (2) Four free half-cylinders (3) Eight free triangles, (4) Eight free half-cylinders, (5) Four fixed triangles, (6) Four fixed half-cylinders, (7) Eight fixed triangles, and (8) Eight fixed half-cylinders.

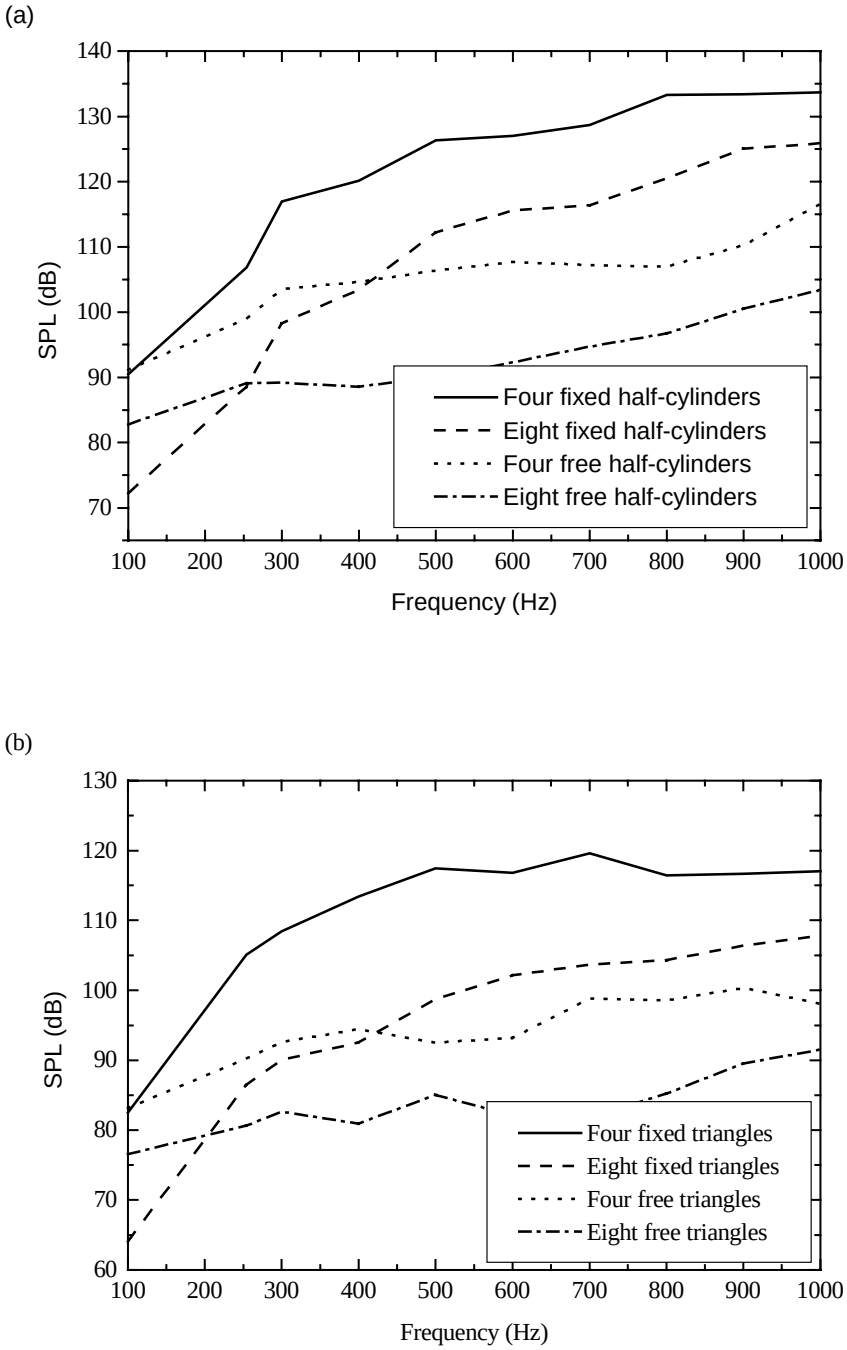

Figure 4.21: Sound pressure level vs. frequency generated by various smart foam array configurations excited at 300 V_{rms} while positioned in rigid duct with anechoic termination (a) Smart foam with embedded PVDF shaped as half-cylinders (b) Smart foam with embedded PVDF shaped as triangles.

4.15 Summary

A numerical formulation of the composite smart foam actuator was established in this chapter. The composite operates in an acoustic environment and requires proper modeling of porous materials, acoustic and piezoelectric systems.

Prior to presenting the numerical smart foam simulations, the analytical Biot theory for the modeling of a porous sound absorbing acoustic foam used in this study was presented. It revealed the unique characteristics of the dual-phase foam used in noise control applications relative to homogeneous elastic materials in that:

(1) the wavepeed of the compressional wave associated with the frame, P_1, is the fastest of the three wavetypes and is virtually independent of frequency.

(2) the compressional wave associated with the fluid, $P_{2,}$ has the highest attenuation per wavelength up to 40000 Hz and provides the bulk of the acoustic energy dissipation of the three wavetypes.

(3) the shear wave, $P_{3,}$, travels only in the solid phase of the foam.

(4) the presence of the fluid in the pores of the material increases the stiffness of the bulk material.

(5) compared to an equivalent rigid porous material, the finite frame elasticity has the effect of reducing the phase velocity of the airborne wave.

A numerical foam model using linear triangular elements was established and comparison of the foam displacement generated by a mechanical force showed excellent agreement with the Biot model predictions. Linear triangular elements were implemented to formulate an acoustic numerical model of an air-filled rigid duct excited by an oscillating piston. Excellent agreement was obtained when the pressure within the duct was compared to that predicted by the analytical solution. A piezoelectric numerical model was constructed using simple axial elements and verified by published analytical solutions on curved piezoelectric actuators. Once the numerical modeling of the acoustic foam, air and piezoelectric material was completed and verified with analytical solutions, a smart foam code programmed in MATLAB® by the author allowed investigation of the acoustic response of either “cylindrical or triangular” shaped piezoelectric actuators

embedded within the foam to identify the optimal configuration for low frequency sound control. It was determined that a series of cylindrically curved PVDF actuators with fixed boundary conditions offered the highest low frequency sound output. It is further evident that the radius of the embedded PVDF actuators should be as large as the physical constraints imposed by the finite thickness of the foam will permit.